



## Eulerian-Lagrangian finite element modelling of food flow-fracture in the stomach to engineer digestion



C.G. Skamniotis<sup>a,\*</sup>, Cathrina H. Edwards<sup>b</sup>, Serafim Bakalis<sup>c</sup>, Gary Frost<sup>d</sup>, M.N. Charalambides<sup>a</sup>

<sup>a</sup> Department of Mechanical Engineering, Imperial College London, London SW7 2AZ, UK

<sup>b</sup> Food and Health, Quadram Institute Bioscience, Colney, Norwich NR4 7UA, UK

<sup>c</sup> Department of Chemical and Environmental Engineering, Faculty of Engineering, University of Nottingham, Nottingham NG7 2RD, UK

<sup>d</sup> Nutrition and Dietetic Research Group, Faculty of Medicine, Imperial College, University of London, London W12 0NN, UK

### ARTICLE INFO

**Keywords:**

Food bolus flow-breakdown  
Food bolus viscoplastic-damage law  
Wire cutting modelling  
Eulerian finite element analysis  
Peristaltic waves  
Pyloric sphincter

### ABSTRACT

Highly processed foods tend to form weak structures which breakdown rapidly in the gastrointestinal (GI) tract, often causing negative effects on human metabolism and health. Developing healthier foods has been limited by the lack of understanding of how foods are digested. Through computational modelling we reveal mechanical gastric food breakdown phenomena and relate food mechanical properties with performance during critical initial digestion stages. Our model relies strictly on a viscoplastic-damage constitutive law, calibrated via rheological experiments on an artificial biscuit bolus and validated by simulating cutting tests. Simulations suggest that bolus separation during bolus backward extrusion and/or indentation by peristaltic waves, and, bolus agglomeration due to hydrostatic compression near the pylorus, are two competing phenomena that can influence the bolus free surface to volume ratio. This showcases the importance of including mechanical aspects of breakdown when designing foods for controlled chemo-mechanical breakdown and associated nutrient release rates.

### 1. Introduction

The evolution of food structure within the digestive tract influences drastically the metabolism and health of individuals (Singh, Ye, & Ferrua, 2015). In many highly processed carbohydrate-rich foods, the original cellular structure is lost prior to digestion. Since the physico-chemical state of starch is strongly linked to glycaemic index (Brouns et al., 2005), such foods breakdown fast in the GI tract, eliciting a high postprandial glycaemic index (Björck, Granfeldt, Liljeberg, Tovar, & Asp, 1994; Brand, Nicholson, Thorburn, & Truswell, 1985) and having a negative impact on appetite regulation; they often cause detrimental effects to glucose homeostasis (Schwingsackl & Hoffmann, 2013) which increases the risk of non-communicable diseases (NCDs) e.g. obesity and type 2 diabetes (Augustin, Franceschi, Jenkins, Kendall, & La Vecchia, 2002; Karthikeyan, Salvi, Corradini, Ludescher, & Karwe, 2019; Poti, Braga, & Qin, 2017). In contrast, foods that have a lower glycaemic index display positive impact on human health and may also serve in enhancing satiety, stabilizing blood sugar levels and reducing insulin resistance (Bahado-Singh, Riley, Wheatley, & Lowe, 2011).

To satisfy specific nutritional needs, promote various physiological functions and prevent/manage NCDs, food structures can be

reformulated to breakdown in a controlled manner (Lundin, Golding, & Wooster, 2008; Overduin, Guérin-Deremaux, Wils, & Lambers, 2015; Skamniotis, Patel, Elliott, Charalambides, 2018). Nevertheless, although some correlations between food manufacturing/preparation methods and metabolic response are established (Johansson, Gutiérrez, Landberg, Alminger, & Langton, 2018; Koistinen et al., 2018; Ozvural & Bornhorst, 2018; Rush, Jantzi, Dupak, Idziak, & Marangoni, 2008), the more fundamental link between food structure and metabolic behaviour is poorly understood (Drechsler & Ferrua, 2016; Kong & Singh, 2008). Tools that can provide comprehensive understanding, evaluation and prediction of structure breakdown, transformation and subsequent in-vivo response are therefore in urgent need.

Digestion response has been investigated under well-controlled conditions that mimic realistic GI biochemical processes through in-vitro models (Bohn et al., 2018; Brodkorb et al., 2019). Most of these, however, did not account for the larger scale, in-vivo physical/mechanical processes i.e. gastric mixing, food bolus deformation and fracture (Drechsler & Ferrua, 2016; Guerra et al., 2012). Undoubtedly, the evolution of food structure during comminution within the fluidic GI environment, is an important aspect during the oral and gastric phases where the food pieces are larger and less diluted (Le Feunteun,

\* Corresponding author.

E-mail addresses: [skamniot@gmail.com](mailto:skamniot@gmail.com), [c.skamniotis13@ic.ac.uk](mailto:c.skamniotis13@ic.ac.uk) (C.G. Skamniotis), [m.charalambides@imperial.ac.uk](mailto:m.charalambides@imperial.ac.uk) (M.N. Charalambides).

| <b>Nomenclature</b>           |  |
|-------------------------------|--|
| <i>Abbreviations</i>          |  |
| GI                            | gastrointestinal tract   |
| NCD                           | non-communicable disease   |
| FE                            | finite elements  |
| 2D                            | two-dimensional  |
| 3D                            | three-dimensional  |
| ACW                           | antral contraction waves   |
| CFD                           | computational fluid dynamics   |
| PBS                           | phosphate buffered saline  |
| <i>Symbols: Mechanical</i>    |  |
| $F$                           | external force (N).  |
| $\delta$                      | external displacement (mm).  |
| $u$                           | nodal translation (mm).  |
| $\theta$                      | nodal rotation (rad).  |
| $\varepsilon$                 | true (Hencky) normal strain.   |
| $\gamma$                      | shear strain.  |
| $\sigma$                      | true (Cauchy) stress (kPa).  |
| $\tau$                        | shear stress.  |
| $p$                           | hydrostatic pressure (kPa).  |
| $\eta$                        | stress triaxiality.  |
| $\mu$                         | friction coefficient.  |
| $D$                           | damage variable.   |
| $W$                           | strain energy density ( $\text{mJ/mm}^3$ ).  |
| $\hat{I}_1$                   | deviatoric first principal deformation invariant.                                    |
| $\hat{I}_2$                   | deviatoric second principal deformation invariant.                                   |
| $\hat{I}$                     | deformation invariant related quantity.  |
| $\zeta$                       | deformation invariant related quantity.  |
| <i>Symbols: Material</i>      |  |
| $M_{\%}$                      | percentage moisture content (w/w).   |
| $\rho$                        | density ( $\text{g/mL}$ ).   |
| $E$                           | Elastic Modulus (kPa).   |
| $K$                           | Bulk Modulus (kPa).  |
| $\nu$                         | Poisson's ratio.   |
| $\sigma_y$                    | yield onset stress (kPa).  |
| $G_c$                         | fracture toughness ( $\text{mJ/mm}^2$ ).   |
| $\psi$                        | initial shear modulus (kPa).   |
| $\lambda_m$                   | locking stretch.   |
| $\alpha$                      | polymer chain interaction parameter.   |
| $\beta$                       | mixture parameter between deviatoric first and second deformation invariants.        |
| $J_{el}$                      | elastic volume ratio.  |
| $\mathcal{H}$                 | hardening modulus (kPa).   |
| $m$                           | hardening exponent.  |
| <i>Symbols: Geometrical</i>   |  |
| $D$                           | specimen diameter (mm).  |
| $H$                           | specimen height (mm).  |
| $W$                           | specimen width (mm).   |
| $T$                           | specimen thickness (mm).   |
| $A$                           | specimen cross-sectional area (mm).  |
| $D$                           | cylindrical cutting diameter (mm).   |
| $d$                           | cutter diameter (mm).  |
| $\varepsilon$                 | wedged shaped Eulerian domain radius (mm).   |
| $C$                           | relative occlusion.  |
| $\lambda$                     | wavelength (mm).   |
| $a$                           | wave shape parameter.  |
| $k$                           | relative distance of subsequent ACWs.  |
| $\xi$                         | ACW local position function (mm).  |
| <i>Symbols: Spatial</i>       |  |
| $x$                           | longitudinal ( $X$ -axis) coordinate (mm).   |
| $j$                           | curvilinear ( $\mathcal{J}$ -axis) coordinate (mm).                                  |
| $r$                           | radial ( $R$ -axis) coordinate (mm).   |
| $x'$                          | local longitudinal ( $X'$ -axis) coordinate (mm).                                    |
| <i>Symbols: Time</i>          |  |
| $\Delta t$                    | physical time duration (s).  |
| $t$                           | time instance (s).   |
| <i>Accents – superscripts</i> |  |
| $\cdot$                       | denotes rate (1/s).  |
| $'$                           | local coordinate system property.  |
| <i>Subscripts</i>             |  |
| $eq$                          | denotes equivalent (Von Mises) quantity.   |
| $p$                           | plastic deformation component.   |
| $0$                           | denotes damage onset.  |
| $o$                           | original compression specimen property.  |
| $n$                           | current (deformed) compression specimen property.                                    |
| $\varsigma$                   | original shear rheometry specimen property.  |
| $c$                           | cylindrical cutter/cutting specimen property.  |
| $w$                           | wire cutter/cutting specimen property.   |
| $ch$                          | denotes characteristic stress/strain value.  |
| $X$                           | longitudinal axis/direction and axis/line of symmetry of idealised gastric geometry. |
| $\mathcal{J}$                 | curved axis/line of symmetry of real gastric geometry.                               |
| $Y$                           | vertical axis/direction.   |
| $Z$                           | out-of-plane axis/direction.   |
| $\Theta$                      | angular/circumferential axis/direction.  |
| $R$                           | radial axis/direction.   |
| $i$                           | ACW identifier.  |
| $s$                           | denotes sphincter location.  |
| $F$                           | denotes gastric fundus location.   |
| $P$                           | denotes gastric pyloric location.  |
| $I$                           | denotes beginning of small intestine.  |
| $1$                           | denotes beginning point of Eulerian domain.  |
| $2$                           | denotes end point of Eulerian domain.  |

Mackie, & Dupont, 2020). Recently, Drechsler et al. (Drechsler & Bornhorst, 2018; Drechsler & Ferrua, 2016) extracted food breakdown data i.e. increase of bolus free surface area over volume ratio, under both the individual and combined activity of the mechanical and chemical processes. The data were linked to measurements of the degradation of bolus mechanical properties i.e. elastic modulus, fracture strength, toughness, as a function of chemical activity, bringing us closer to understanding the link between key material properties and

in-vivo food performance. Nevertheless, the model assumed that mechanical breakdown involves purely compressive forces as a result of the Antral Contraction Waves (ACWs) of the stomach wall, which could prove a major shortcoming; ACWs as well as the surrounding gastric liquid flow and pressure could generate tensile forces on the bolus. Such physiological conditions have been accounted for in dynamic gastric in-vitro models (Dupont et al., 2019, Ménard et al., 2014, Minekus, Marteau, & Havenaar, 1995) and peristaltic duodenal models

(Avantaggiato, Havenaar, & Visconti, 2003; Kong & Singh, 2010). However, their results proved largely sensitive to the assumptions/simplifications of the in-vivo ACW characteristics (Hur, Lim, Decker, & McClements, 2011) and discrepancies were found amongst research groups (Yoo & Chen, 2006). Simultaneously, in-vivo studies often involve limitations due to prohibitive costs and ethical considerations (Bornhorst, Gouseti, Wickham, & Bakalis, 2016; Ferrua & Singh, 2010).

The above challenges associated with in-vivo and in-vitro techniques, have led researchers to develop *in-silico* – mechanistic models as modern-alternative means of contributing to the understanding of food digestion (Feinle, Kunz, Boesiger, Fried, & Schwizer, 1999; Ferrua, Kong, & Singh, 2011; Le Feunteun et al., 2020; Moxon, Gouseti, & Bakalis, 2016). Yet, although much related work has been performed in the pharmaceutical sector (Abrahamsson, Albery, Eriksson, Gustafsson, & Sjöberg, 2004; Koziolek, Grimm, Garbacz, Kühn, & Weitschies, 2014; Walter-Sack, De Vries, Nickel, Stenzhorn, & Weber, 1989), relevant literature in foods is limited to a small number of reports (Pal, Brasseur, & Abrahamsson, 2007; Ferrua & Singh, 2010; Kozu et al., 2010; Xue, Pontin, Zok, & Hutchinson, 2010; Ferrua et al., 2011; Imai et al., 2013; Ferrua, Xue, & Singh, 2014; Harrison, Cleary, Sinnott, Hari, Bakalis, & Harrison, 2015; Alokaily, Feigl, & Tanner, 2019), which have mainly focused on the flow patterns of liquid meals upon the application of ACWs based on Computational Fluid Dynamics (CFD). Therefore, aspects such as the stomach posture (Imai et al., 2013), meal rheology (Ferrua et al., 2014), effect of gastric wall - fluid slip conditions (Ferrua et al., 2011) and Reynolds number (Alokaily et al., 2019) on mixing rate and velocity fields of digesta, have been mainly investigated. As a matter of fact, the physics-mechanics of transformation in solid-like foods during digestion remains yet to be explored. In particular, although solid meals have been modelled during the primary oral phase of digestion via Finite Element and meshfree methods i.e. food oral breakdown models (Harrison et al., 2014b; Harrison & Cleary, 2014; Harrison, Cleary, Eyres, Sinnott, & Lundin, 2014a; Skamniotis, Elliott, & Charalambides, 2019; Skamniotis, Patel, Charalambides, & Elliott, 2016; Mohammed et al., 2019), their behaviour in the stomach has received minor attention. This is despite the fact that gastric breakdown is known to be a major determinant of gastric emptying, which effectively dictates the nutrient uptake kinetics (Kong & Singh, 2008; Le Feunteun et al., 2014; Le Feunteun et al., 2020; Mackie, Rafiee, Malcolm, Salt, & van Aken, 2013; Marciani et al., 2013).

Undoubtedly, *in-silico* – mechanistic modelling of solid food breakdown under the combined activity of mechanical forces, hydration and enzymes/acids, consists a complex multidisciplinary task. A major scientific and technological challenge is to establish a theoretical and numerical basis able to capture both the individual phenomena that take place at different characteristic length scales in the GI tract, as well as the coupling-link mechanisms between these phenomena. Another challenge relates to the need for suitable in-vivo data towards validating the physiological relevance of *in-silico* predictions (Le Feunteun et al., 2020), thus providing the essential building blocks for the continuous development of *in-silico* models. A limiting factor, so far, is that an in-vivo database is not available to the model developers, which is suggested (Le Feunteun et al., 2020) to hinder the identification of suitable characteristic digestion variables within in-vivo data reported from authors of various disciplines. Conversely, the required input parameters, features and limitations associated with computational modelling tools have not been easily communicable to experimentalists and physiologists (Le Feunteun et al., 2020). All the above showcase the need for closer collaboration between experts in modelling and experiments, towards gathering and combining in-vivo, in-vitro and *in-silico* knowledge that will support further advances in *in-silico* – mechanistic modelling of digestion.

This report contributes to the challenges mentioned, by providing detailed information on aspects which have not received attention so far. We produce this information through the process of developing a novel *in-silico* gastric processing Finite Element (FE) model, able to

explore and reproduce phenomena underpinning the large scale mechanical gastric breakdown of solid foods. The main advantage of our *in-silico* modelling approach is that the input parameters i.e. the food constitutive law, rely on intrinsic material properties measured by standardised mechanical tests that are readily reproducible in mechanical testing laboratory testing i.e. uniaxial compression (also known as lubricated squeezing flow) and shear rheometry. Although our experimental-modelling analysis uses an artificial biscuit bolus as a food model system, our entire research strategy is shown to be of use in studying a range of solid food macroscopic breakdown scenarios, especially for the initial stages of digestion and for food boluses with a pronounced solid texture i.e. considerable resistance against deformation; for these resistant systems, the mechanical component of breakdown is deemed particularly important. The validity of our numerical results is verified by using the food constitutive law to model additional wire cutting and cylindrical cutting experiments. At this stage, our FE model captures the mechanical component of breakdown alone, in the absence of hydrodynamic and bio-chemical processes. Nonetheless, the pronounced complexity of coupled mechanical-hydrodynamic-bio-chemical breakdown, is why the authors believe that studying mechanical flow-breakdown alone adds significant value, since also the latter has not been studied rigorously before. As a result, our model here provides for the first time an extensive evaluation of solid mechanics phenomena in the process of digestion, providing a strong foundation for more elaborate analyses of food breakdown under multiple gastric activities.

The study is structured as follows. Section 2 describes the bolus material preparation and characterisation tests, the calibration of the viscoplastic-damage constitutive law, as well as the construction of wire cutting, cylindrical cutting and gastric processing models. Thereafter, Section 3 presents the rheological and cutting experimental data along with the corresponding numerical predictions, followed by the gastric processing simulation results. The merits of our gastric model in establishing links between food mechanical properties and associated gastric food performance are then discussed.

## 2. Materials and methods

### 2.1. Bolus specimen

The solid phase of the bolus consisted of Nairn's fine milled oatcake biscuits (wholegrain oats at 85% w/w, sustainable palm, fruit oil, sea salt, sodium bicarbonate and water at  $2.6 \pm 0.3\%$  w/w), which were firstly grinded (kitchen blender Breville VBL096) and thereafter sieved (Sigma-Aldrich analytical sieve Z289698-1EA, pore size 500  $\mu\text{m}$ ) at particle sizes of less than 0.5 mm. The liquid phase included 30% (v/v) de-ionised water and 70% (v/v) phosphate buffered saline (PBS) solution obtained by dissolving 5 g PBS tablets (Sigma-Aldrich P4417-100TAB) into 200 mL of de-ionised water; the PBS was used to eliminate pH changes in the material during the experimental testing period. From a gastric digestion point of view, the artificial bolus involved two simplifications. Firstly, the realistic scenario of a solid particle size distribution (Chen, 2009; Le Bleis, Chaunier, Montigaud, & Della Valle, 2016; Prinz & Lucas, 1997) imposed by the oral process, was not considered.

Contradictory opinions have been reported on whether solid particles that typically exist within the viscous liquid phase of gastric digesta should be removed prior to rheological measurements (Razdan & Pettersson, 1996; Shelat et al., 2015; Takahashi & Sakata, 2002). Although including the solid particles has eventually prevailed, this often comes at the cost of highly discontinuous (and often inhomogeneous) specimens, based on which net apparent viscosity values can only be extracted (Shelat et al., 2015; Wu, Dhital, Williams, Chen, & Gidley, 2016). The disadvantage of these measurements is that not only they carry the contributions of both solid and liquid phases, but also that these contributions depend on the flow properties, geometry and volume fractions of the individual phases. Specifically, the average solid

particle size and shape is likely to alter the way in which the solid particles (and potentially surrounding liquid phase) undergo shear deformation; therefore, the contribution of the solid phase deformation to the net apparent viscosity data is also expected to change as parameters such as particle size, mechanical properties and their volume fraction change. This further indicates that net apparent viscosity measurements can lead to significant experimental scatter, since the degree of discontinuity between digesta specimens naturally varies i.e. inconsistent particle size-shape-volume fraction. Such high experimental scatter would impede the investigation of the underlying physics taking pace during the gastric process. As a result, net apparent viscosity measurements typically fail to provide intrinsic rheological properties of the solid particles, and of the viscous fluidic phase, separately. Such properties are key information for calibrating suitable material constitutive laws based on which the mechanics of bolus flow-breakdown can be predicted through detailed computational models. Consequently, in order to perform detailed characterisation and computational modelling of the deformation-fracture processes in solid meals, the assumption of a continuum solid bolus was here necessary. This explains why particles of less than 0.5 mm size were used for the solid phase, the size being chosen small enough such that uniform moisture conditions prevail in the bolus, soon after mixing with a liquid phase.

The second simplification associates with using de-ionised water and a PBS solution for the liquid phase instead of more realistic salivary mimics previously employed in the literature (Björklund, Ouwehand, & Forssten, 2011; McClements & Li, 2010; Minekus et al., 2014). This simplification was adopted because the degradation of rheological properties due to the activity of salivary mucin and amylase, would increase remarkably the number of parameters that need to be accounted for in the experimental procedure i.e. reducing reproducibility, as well as would likely increase significantly the amount of scatter in the data. Consequently, combining the mechanical deformation with chemical changes in the material, would hinder the understanding of bolus flow-breakdown purely due to mechanical loading. The significance of the mechanical component of breakdown for the initial stages of digestion here, can be further supported by the fact that the starch in the oatcake biscuit studied here is of granular nature which implies a relatively low accessibility of starch i.e. slow amylase activity (Sozer, Cicerelli, Heiniö, & Poutanen, 2014). More specifically, in these biscuits the starch is mainly in the form of swollen granules but it is not fully gelatinised due to the low moisture conditions during baking. It is expected that the  $\alpha$ -glucan chains of starch are accessible to amylase,

but hydrolysed at a slower rate than in a fully gelatinised state (amorphous starch).

Mixing of the solid-liquid phases was performed as shown in Fig. 1(a) (6-pin planetary mixer previously used in (Mohammed, Tarleton, Charalambides, & Williams, 2013)), such that total moisture contents (dry/liquid weight ratios),  $M_{\%}$ , of 40%, 50% and 60% are satisfied; within these  $M_{\%}$  contents, the initial 2.6% water content of the solid phase was included. Below  $M_{\%} = 40\%$ , and specifically when  $M_{\%} = 30\%$ , the mixture was overly dry such that a single cohesive bolus mass, such as the one shown in Fig. 1(b) for  $M_{\%} = 50\%$ , could not be formed; such states were not considered to represent a realistic bolus, while also the assumption of a continuum solid material was violated. On the other hand,  $M_{\%} = 70\%$  corresponded to a thick fluid, which flows due to gravity, violating the assumption of a solid bolus material. Moulding was used to obtain cylindrical specimens for uniaxial compression in diameter/height ratios,  $D_o/H_o = 20/20\text{mm}$  (see Fig. 1(b)); preliminary tests indicated that the effect of specimen aspect ratio,  $D_o/H_o$ , on the stress-strain results was minor. Moulding was also used to shape cuboidal specimens (see Figs. 1(e), 1(f)) for cylindrical cutting and wire cutting in dimensions (mm):  $H_c \times W_c \times T_c = 20 \times 30 \times 30\text{ mm}$  and  $H_w \times W_w \times T_w = 30 \times 30 \times 20\text{ mm}$ , respectively.

All the experimental data were collected within five consecutive days, by using a freshly mixed material each day which was tested during a maximum of three hours. Material kept sealed for five minutes against material sealed for three hours showed no difference in the compression data. Specimens tested immediately after attachment to the compression platen against specimens tested after being exposed for ten minutes led to a maximum difference of 4% in the average compression forces. Thus, dehydration effects were considered negligible throughout the study, on the basis that the slowest test (0.01/s strain rate in compression) lasted approximately three minutes. Storing and testing of the material correspond to a constant ambient temperature 20 °C and relative humidity 50%. Multiple sensors showed negligible temperature-humidity variation in the laboratory environment.

## 2.2. Rheological tests

### 2.2.1. Uniaxial compression (lubricated squeezing flow)

Uniaxial compression tests, also known as ‘lubricated squeezing flow’ tests, were conducted to obtain equivalent (Von Mises) stress,  $\sigma_{eq}$  (kPa), versus equivalent strain,  $\varepsilon_{eq}$  ( $-/-$ ), data; for uniaxial loading,  $\sigma_{eq}$  and  $\varepsilon_{eq}$  are equivalent to the magnitudes of true (Cauchy) stress,  $\sigma$ ,

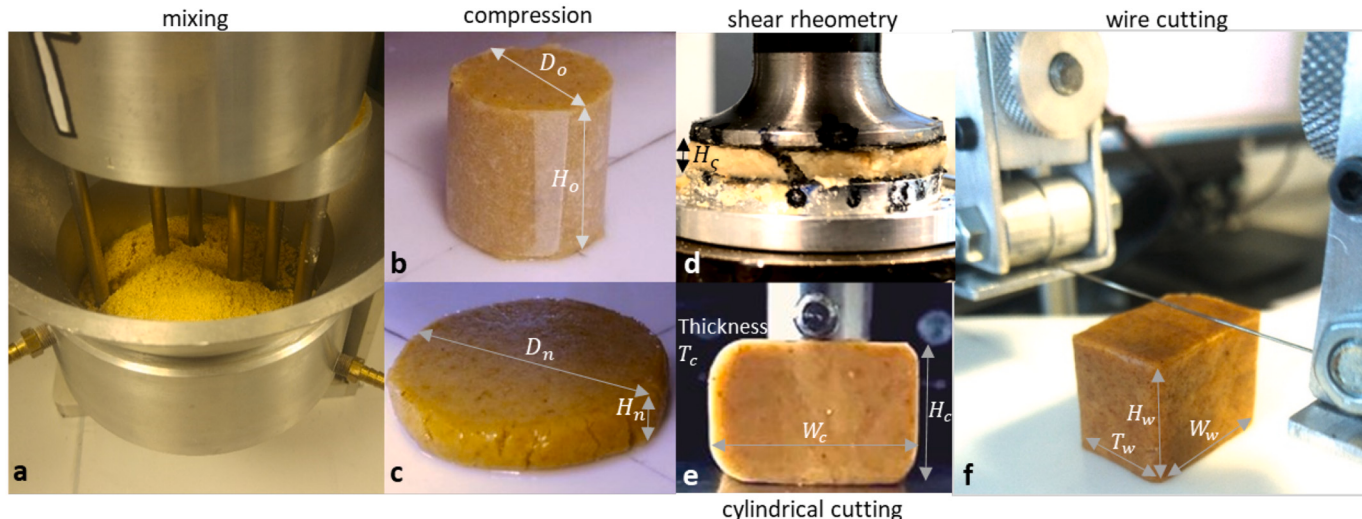


**Fig. 1.** Illustration of mechanical testing methodology. Images show: (a) biscuit-water mixing through planetary pin system, (b) cylindrical moulded specimen for uniaxial compression test (cling film removed prior to testing), (c) specimen at the end of compression test after applying an equivalent strain  $\varepsilon_{eq} = 2$ , (d) shear rheometry test - specimen at shear strain,  $\gamma = 0.8$ , (e) cylindrical cutting test configuration, (f) wire cutting test configuration.

and true (Hencky) strain,  $\epsilon$ , giving:

$$\sigma_{eq} = |\sigma| = \left| \frac{F}{A_i} \right| \quad (1)$$

and

$$\epsilon_{eq} = |\epsilon| = \left| \ln \left( \frac{H_n}{H_o} \right) \right| \quad (2)$$

for applied force,  $F$  (N), current specimen height,  $H_n$  (mm) (see Fig. 1(c)), and current (circular) specimen cross sectional area,  $A_n$  ( $\text{mm}^2$ ), calculated by assuming a perfectly incompressible behaviour (Poisson's ratio,  $\nu = 0.5$  (−/−)) through:

$$H_o A_o = H_n A_n \quad (3)$$

where  $A_o$  ( $\text{mm}^2$ ) is the original specimen cross sectional area. The assumption of incompressibility was justified through optical means (Logitech Pro C920, 30 fps, HD 1920 × 1080) which showed that during compression the specimen's lateral expansion is such that zero volume changes occur. Data were obtained during monotonically increasing applied strain up to  $\epsilon_{eq} = 2$ , at three constant true strain rates,  $\dot{\epsilon}_{eq}$ : 0.01/s, 0.1/s and 1/s (each repeated five times), which span the shear rate range, 0.27/s–0.45/s, that is predicted by Ferrua et al. (Ferrua et al., 2014), to occur in typical Newtonian fluidic meals at the distal stomach region. Stress relaxation data were also measured at three constant strains,  $\epsilon_{eq}$ : 0.1, 0.5 and 1 (each repeated three times), all kept constant for ten minutes, while the initial loading was performed at a rate,  $\dot{\epsilon}_{eq} = 0.01/\text{s}$ . Finally, unloading data were collected by unloading from  $\epsilon_{eq} = 1$  at  $\dot{\epsilon}_{eq} = 0.01/\text{s}$ , after monotonic straining was applied at  $\dot{\epsilon}_{eq} = 0.01/\text{s}$ . In order to minimise undesirable specimen barrelling (Charalambides, Goh, Wanigasooriya, Williams, & Xiao, 2005), the compression platens were smeared with silicon oil of  $10^{-2} \text{ m}^2/\text{s}$  viscosity (Skamniotis, Elliott, & Charalambides, 2017).

## 2.2.2. Shear rheometry

Shear rheometry data were collected based on the parallel plate configuration shown in Fig. 1(d), for three constant shear rates,  $\dot{\gamma}$ : 0.0173/s, 0.173/s and 1.73/s (each repeated three times), which correspond to equivalent rates,  $\dot{\epsilon}_{eq}$ , of: 0.01/s, 0.1/s and 1/s, based on the Von Mises relations:

$$\epsilon_{eq} = \gamma \frac{1}{\sqrt{3}} \quad (4)$$

$$\sigma_{eq} = \tau \sqrt{3} \quad (5)$$

Eqs. (4) and (5) were used to convert the shear stress,  $\tau$  (kPa), and shear strain,  $\gamma$  (−/−), rheometer (TA Instruments AR2000ex) measurements, corresponding to the material at edge of the cylindrical specimen, into  $\sigma_{eq}$  −  $\epsilon_{eq}$  plots. The parallel plate geometry was used due to the need for attaching sand paper (80 grit size) on both upper and lower plates to prevent specimen-plate slippage during shearing (Ng, McKinley, & Padmanabhan, 2007; Tanner, Qi, & Dai, 2008); this would be impractical if the cone-plate configuration was used. A waterproof sand paper (Mirka P80 grit) was chosen as this does not swell when it comes into contact with wet specimens (Mohammed et al., 2013). Extra care was taken by marking a straight vertical line across the outer edge of the specimen as well as the edges the two plates, prior to the tests, as shown in Fig. 1(d). Whether slippage occurs during the tests was qualitatively assessed by observing whether the line was disjointed at the specimen-platen interfaces (Iqbal, Li-Mayer, Lewis, Connors, & Charalambides, 2020), as shown in Fig. 1(d).

Specimens of diameter,  $D_c = 12.5$  mm, were used while the effect of specimen height,  $H_c$  (or equivalently gap size), on the results was investigated by comparing preliminary  $\sigma_{eq}$  −  $\epsilon_{eq}$  results corresponding to three values,  $H_c$ , of: 1 mm, 2 mm and 3 mm (each repeated three times) for a constant rate,  $\dot{\epsilon}_{eq} = 0.1/\text{s}$ . The procedure involves attaching a sufficient mass of bolus material on the lower platen and subsequently

moving the upper platen downwards to reach the prescribed  $H_c$ ; the excess material is removed via a spatula prior to the tests. Whether the level of material pre-straining influences the results was investigated by using a constant  $H_c = 2$  mm and  $\dot{\epsilon}_{eq} = 0.1/\text{s}$  and comparing  $\sigma_{eq}$  −  $\epsilon_{eq}$  data for varying initial bolus mass attached between the plates i.e. between 2 g, 5 g, and 10 g; these values correspond to extreme cases i.e. 10 g leads to a large excess of material while 2 g leads to practically no material excess. On the other hand, whether the duration of material relaxation prior to the tests influences the results was assessed by varying the specimen equilibration time between one minute, five minutes and twenty minutes and comparing the corresponding  $\sigma_{eq}$  −  $\epsilon_{eq}$  data; for five minutes and twenty minutes the specimen together with parts of the upper and lower plate fixtures were gently wrapped in cling film to prevent potential drying effects.

## 2.3. Cylindrical/wire cutting

Cylindrical cutting and wire cutting involved a rigid cylindrical cutter with diameter,  $d_c = 5$  mm (see Fig. 1I) and a sufficiently taut wire with diameter,  $d_w = 0.5$  mm (see Fig. 1(f)), respectively; a rigid platen was used for specimen support. The wire cutting apparatus shown in Fig. 1(g) has been previously used in (Goh, Charalambides et al., 2005, Gamonpilas, Charalambides, & Williams, 2009). Four cylindrical/wire cutting speeds,  $\dot{\delta}$ , of 0.1 mm/s, 1 mm/s, 2.5 mm/s and 10 mm/s (each repeated three times), were applied up to a maximum cylinder displacement,  $\delta = 18$  mm. The speed,  $\dot{\delta} = 2.5$  mm/s, is relevant to the average in-vivo ACW speed of 2.7 mm/s measured by Kwiatek et al. (Kwiatek et al., 2006).

## 2.4. Computational modelling

### 2.4.1. Outline

Computational modelling primarily required calibration of a suitable bolus constitutive law based on the rheological  $\sigma_{eq}$  −  $\epsilon_{eq}$  data. Our models were investigated for  $M\% = 50\%$ , because at this moisture content the bolus displayed both excessive plastic flow as well as micro-cracking. The constitutive law provides the input material parameters in Finite Element (FE) models of cylindrical cutting, wire cutting as well as gastric processing. The latter also required a constitutive law describing the mechanical response of the gastric wall, as well as an algorithm for implementing ACWs. All simulations were performed based on a Coupled Eulerian-Lagrangian (CEL) FE scheme and the dynamic-explicit solver of the commercial FE software ABAQUS (Simulia, 2013), while ensuring that quasi-static conditions apply i.e. inertial forces and the associated material density parameter do not influence the solution (Skamniotis et al., 2016). Descriptions of theoretical and practical aspects of the Eulerian FE formulation are available in (Benson & Okazawa, 2004; Simulia, 2013).

### 2.4.2. Constitutive law for gastric wall

The stomach wall was set to obey a hyperelastic constitutive law (Fontanella et al., 2019) based on the following Van der Waals (VDW) strain energy density potential,  $W$ , (mJ/mm<sup>3</sup>), widely used in rubbery polymers (Simulia, 2013):

$$W = \psi \left\{ -(\lambda_m^2 - 3)[\ln(1 - \zeta) + \zeta] - \frac{2}{3}\alpha \left( \frac{\tilde{\lambda} - 3}{2} \right)^{\frac{3}{2}} \right\} + \frac{K}{2} \left( \frac{J_{el}^2 - 1}{2} - \ln J_{el} \right) \quad (6)$$

where  $\psi$  (kPa) is the initial shear modulus,  $\lambda_m$  (−/−) defines the stretch ratio/deformation beyond which the corresponding stress experienced by the polymer increases sharply with further deformation, also known as 'locking stretch',  $\alpha$  (−/−) represents the degree of

entanglement between the chains of the polymer (influences the non-linearity of the stress-strain response),  $J_{el}$  ( $-/-$ ) is the elastic volume ratio ( $J_{el} = 1$  for incompressible response) as a measure of volumetric elastic strain, and  $K$  (kPa) is the initial bulk modulus that relates to the Poisson's ratio,  $\nu$  and  $\psi$  through:

$$\nu = \frac{3K/\psi - 2}{6K/\psi + 2} \quad (7)$$

The quantities  $\tilde{I} = (1 - \beta)\hat{I}_1 + \beta\hat{I}_2$  and  $\zeta = \sqrt{\frac{\tilde{I}-3}{\lambda_m^2-3}}$ , depend on the deviatoric first,  $\hat{I}_1$ , and second,  $\hat{I}_2$ , principal deformation invariants, as a function of the invariant mixture parameter,  $\beta$  ( $-/-$ ).

The ACWs were applied in terms of prescribed displacements histories on each node/element of the gastric wall, giving rise to a displacement controlled gastric processing. As a result, the aforementioned VDW law parameters and associated gastric wall stresses generated when the ACWs are applied, do not affect the bolus deformation-fracture response here. Thus, although the VDW parameters were necessary for the numerical implementation of the constitutive law for the gastric wall, the selected values of the parameters and their physical meaning were not physically important in this study. While this allowed for an arbitrary choice of the VDW parameters here, it was essential that these parameters also satisfy the following two criteria. Firstly, the Drucker's material stability condition (Drucker, 1957) must be always satisfied to ensure reasonable material response and numerical convergence. Secondly, a reasonable ratio between the deviatoric and volumetric contributions to the total value of  $W$ , must be defined. Equivalently, this implies that the ratio of  $K/\psi$  ( $-/-$ ) should not be very high or very low. Specifically, large ratios i.e.  $K/\psi > 100$ , generally result in noisy solutions for dynamic-explicit FE analyses (Simulia, 2013), while on the other hand, very low  $K/\psi$  ratios were found to result in significant contact penetration effects i.e. very low contact stiffness. Based on the above requirements, the VDW parameters were chosen:  $\psi = 100$  kPa,  $\lambda_m = 100$ ,  $\alpha = 0.5$ ,  $\beta = 0$  (no  $\hat{I}_2$  dependence) and  $K = 2000$  kPa, leading to  $K/\psi = 20$  and Poisson's ratio,  $\nu = 0.475$ . An arbitrary density of  $\rho = 1$  g/mL (1E-07 tn/mm<sup>3</sup> for ABAQUS) was used.

#### 2.4.3. Bolus constitutive law

**2.4.3.1. Viscoplastic-damage law for oatcake bolus.** Amongst several constitutive laws utilised previously for soft solid foods (Gamonpilas et al., 2009; Mohammed et al., 2013; Skamniotis et al., 2017), the coupled viscoplastic-damage law was deemed the most suitable here. The law mainly consists of an initially elastic regime, governed by a rate independent elastic modulus,  $E$  (kPa), followed by a rate dependent plastic regime; this is referred here as 'viscoplastic law' (no damage). The latter can be set to degrade to zero stress as soon as an equivalent plastic strain,  $\varepsilon_{peq_0}$ , and a stress triaxiality,  $\eta_0$ , are exceeded (see (Skamniotis, Elliott, & Charalambides, 2018) for details). Both the viscoplastic and viscoplastic-damage laws will be illustrated in Fig. 4(c), along with experimental data (data fitting to be discussed in Section 3.1.2). For known hydrostatic pressure,  $p$  (kPa), and equivalent (Von Mises) stress,  $\sigma_{eq}$ , the stress triaxiality,  $\eta$  ( $-/-$ ), variable was used to differentiate between stress states, based on:

$$\eta = -\frac{p}{\sigma_{eq}} \quad (8)$$

which yields  $\eta = -1/3$  in uniaxial compression,  $\eta = 0$  in simple shear (no pressure) and  $\eta = 1/3$  in uniaxial tension. For identical stresses in two directions Eq. (8) also implies that  $\eta = -2/3$  and  $\eta = 2/3$  in equibiaxial compression and tension, respectively. By also applying stress in a third direction, Eq. (8) implies that the absolute value of  $\eta$  can exceed unity i.e.  $|\eta| > 1$ , and theoretically reach infinity i.e.  $|\eta| \rightarrow \infty$  for the idealised scenarios of hydrostatic compressive and/or tensile states (due to  $\sigma_{eq} = 0$ ). On the other hand, a damage variable,  $D$  ( $-/-$ ), was used to differentiate between an undamaged ( $D = 0$ ) and a

fully damaged ( $D = 1$  and  $\sigma_{eq} = 0$ ) material state. Full damage was set to occur abruptly here, such that the stress degrades to zero as soon as damage onset is met i.e. as soon as  $\varepsilon_{eq} > \varepsilon_{peq_0}$  and simultaneously  $\eta > \eta_0$ . The latter implies that beyond damage onset, no additional energy is dissipated within an element of a FE mesh; this condition can be considered to be equivalent to a zero material fracture toughness,  $G_c = 0$  mJ/mm<sup>2</sup>. The damage onset parameters  $\varepsilon_{peq_0}$  and  $\eta_0$  for our material, were calibrated inversely by simulating the cylindrical cutting experiment (to be described in Section 3.2.3); note that for  $\eta < \eta_0$  damage was not allowed to occur regardless of the strain level, such that unrealistic material stiffness degradation for compressive states was prevented (Skamniotis et al., 2017; Skamniotis et al., 2019). This strategy, together with the significance of damage onset parameters in simulating bolus cutting are fully described by the authors in (Skamniotis and Charalambides, 2020). An extensive description of other aspects related to the numerical implementation of the viscoplastic-damage is available in (Skamniotis, n.d.).

The viscoplastic law was calibrated as follows: firstly the elastic modulus,  $E$ , is measured; thereafter the rheological  $\sigma_{eq} - \varepsilon_{eq}$  test data are converted into  $\sigma_{eq} - \varepsilon_{peq}$  data through decomposition of  $\varepsilon_{eq}$  into the elastic,  $\varepsilon_{eq}$ , and plastic,  $\varepsilon_{peq}$ , components, based on:

$$\varepsilon_{eq} = \varepsilon_{eq} + \varepsilon_{peq} \Leftrightarrow \varepsilon_{peq} = \varepsilon_{eq} - \frac{\sigma_{eq}}{E} \quad (9)$$

Instead of  $\nu = 0.5$  which was considered to be the true Poisson's ratio in our material, a value of  $\nu = 0.49$  is used in order to satisfy the recommended limit,  $K/\psi < 100$ , for a dynamic-explicit analysis (REF). Specifically, for the experimentally measured,  $E = 100$  kPa (to be presented in Section 3.1.2) here, a  $\nu = 0.49$  leads to  $K/\psi = 49.66$ ; this is based on Eq. (7), as well as the fundamental relations,  $K = \frac{E}{3(1-2\nu)}$  and  $\psi = \frac{E}{2(1+\nu)}$ . Lastly, the true material density,  $\rho = 1.1E-07$  tn/mm<sup>3</sup> = 1.1 g/mL was used, calculated via weight measurements of the compression specimens shown in Fig. 1b.

**2.4.3.2. Hypothetical elastic-plastic J law.** The elastic-plastic theory was also used to model the response of a hypothetical bolus, in which stress increases non-linearly with strain, exhibiting a 'J' shaped  $\sigma_{eq} - \varepsilon_{eq}$  curve; rate dependency and damage were not included here. This type of stress-strain behaviour simultaneously resembles a typical hyperelastic/rubber-like response which has been reported for cheese (Goh, Charalambides et al., 2005), bread dough (Mohammed et al., 2013) and starch gels (Gamonpilas et al., 2009). The difference here is that plastic strain is considered to dominate during deformation, as opposed to the classical hyperelastic response where the elastic strain dominates and plasticity is absent. Based on these characteristics, the hypothetical bolus behaviour here is referred as 'hypothetical elastic-plastic J law'. An initial linear elastic regime was used, followed by a rate independent non-linear plastic hardening regime, according to:

$$(a) \sigma_{eq} = E\varepsilon_{eq}, \sigma_{eq} \leq \sigma_y \\ (b) \sigma_{eq} = \sigma_y + \mathcal{H}\varepsilon_{eq}^m, \sigma_{eq} > \sigma_y \quad (10)$$

where  $\sigma_y$  (kPa) is the yield onset stress,  $m$  ( $-/-$ ) is the hardening exponent and  $\mathcal{H}$  (kPa) is the hardening modulus calibrated by combining Eqs. (9) and (10b) to give:

$$A = \frac{\sigma_{eqch} - \sigma_y}{\left(\varepsilon_{eqch} - \frac{\sigma_{eqch}}{E}\right)^m} \quad (11)$$

where  $E$ ,  $\sigma_{eqch}$  and  $\varepsilon_{eqch}$  are respectively the elastic modulus, a characteristic stress and a corresponding characteristic strain, all taken from the experimental  $\sigma_{eq} - \varepsilon_{eq}$  curve of the oatcake bolus for the rate  $\dot{\varepsilon}_{eq} = 0.01/s$ ; the latter guarantees similar stress magnitudes between the hypothetical elastic-plastic J law and the viscoplastic law (and thus also viscoplastic-damage law) of the oatcake bolus.

#### 2.4.4. Cylindrical and wire cutting models

Figs. 2(a-b) and 2(c) illustrate the 3D and pseudo-2D cylindrical cutting models while Figs. 2(d-e) refer to the pseudo-2D wire cutting model. The pseudo-2D models in Figs. 2(c) and 2(d-e) use a single element in the out-of-plane direction (Puls, Klocke, & Lung, 2014), in order to idealise the cylindrical and wire cutting tests, respectively, as 2D (two-dimensional) problems with plane strain conditions; note that the current Eulerian FE analysis is not applicable for 2D elements (Simulia, 2013). In general, 2D analysis can typically capture the experimental (true) force-displacement response measured at the cylindrical/wire cutting tool with fair accuracy, provided that the specimen is thick enough (in the z direction i.e. see Fig. 2(a)) such that plane strain conditions apply in most of its volume. However, by principle such conditions do not apply at the specimen's free/external surfaces where the stress components normal to these surfaces must be zero i.e. plane stress conditions prevail instead. These conditions can be modelled only in 3D space i.e. here the 3D model in Figs. 2(a-b). In addition, previous study in starch foods (Skamniotis et al., 2017) has highlighted the necessity of using 3D models for capturing surface micro-cracking and fracture phenomena during cylindrical cutting.

All models consist of a cuboidal Eulerian domain/box which encloses the original (Eulerian) bolus specimen, as well as the platen and cylindrical/wire cutters which are modelled as discrete rigid (Lagrangian) shells. Cutting was applied via specifying translation of the cylinder/wire in the -Y direction at various rates,  $\dot{\delta}$  (mm/s), while constraining all the other degrees of freedom; fixed conditions were

applied in the supporting platen. Contact was modelled via the ABAQUS general contact algorithm (Simulia, 2013) based on a friction coefficient,  $\mu = 0.9$ , which was found to give the best overall experimental-model agreement. The 3D cylindrical cutting model (Figs. 2(a-b)) consists of only half of the cylindrical cutting test assembly, such that X – Y is a symmetry plane with the following Z-symmetry boundary conditions: zero translational velocity along Z axis ( $\dot{u}_z = 0$ ) and zero rotational velocities about X and Y axes ( $\dot{\theta}_X = \dot{\theta}_Y = 0$ ) were also enforced; modelling a quarter of the cylindrical cutting test assembly by also taking advantage of the symmetry about the Y – Z plane (X-symmetry boundary conditions), led to unphysical results for the Eulerian FE analysis here. The plane strain condition in the pseudo-2D models (Figs. 2(c-d)) was enforced by applying Z-symmetry (as above) in both -Z and +Z bounding faces of the Eulerian domain (denoted in Figs. 2(c-d)); similarly to the 3D cylindrical cutting model, it was not possible to model half of the pseudo-2D model. A 3D wire cutting model was not considered due to an exceedingly large number of elements (mesh size) required to discretise a Eulerian domain which fulfils the following two requirements: (a) captures details of deformation-fracture with a sufficient discretisation level in the regions surrounding the wire i.e. at the moving cutting tip, and, (b) encloses the whole volume of the wire cutting specimen.

The mesh size requirements were reduced further in all models, by utilising a 'Eulerian mesh motion' algorithm (Simulia, 2013), such that the Eulerian domain can translate and expand/contract depending on the motion-deformation of the bolus. Domain expansion/contraction

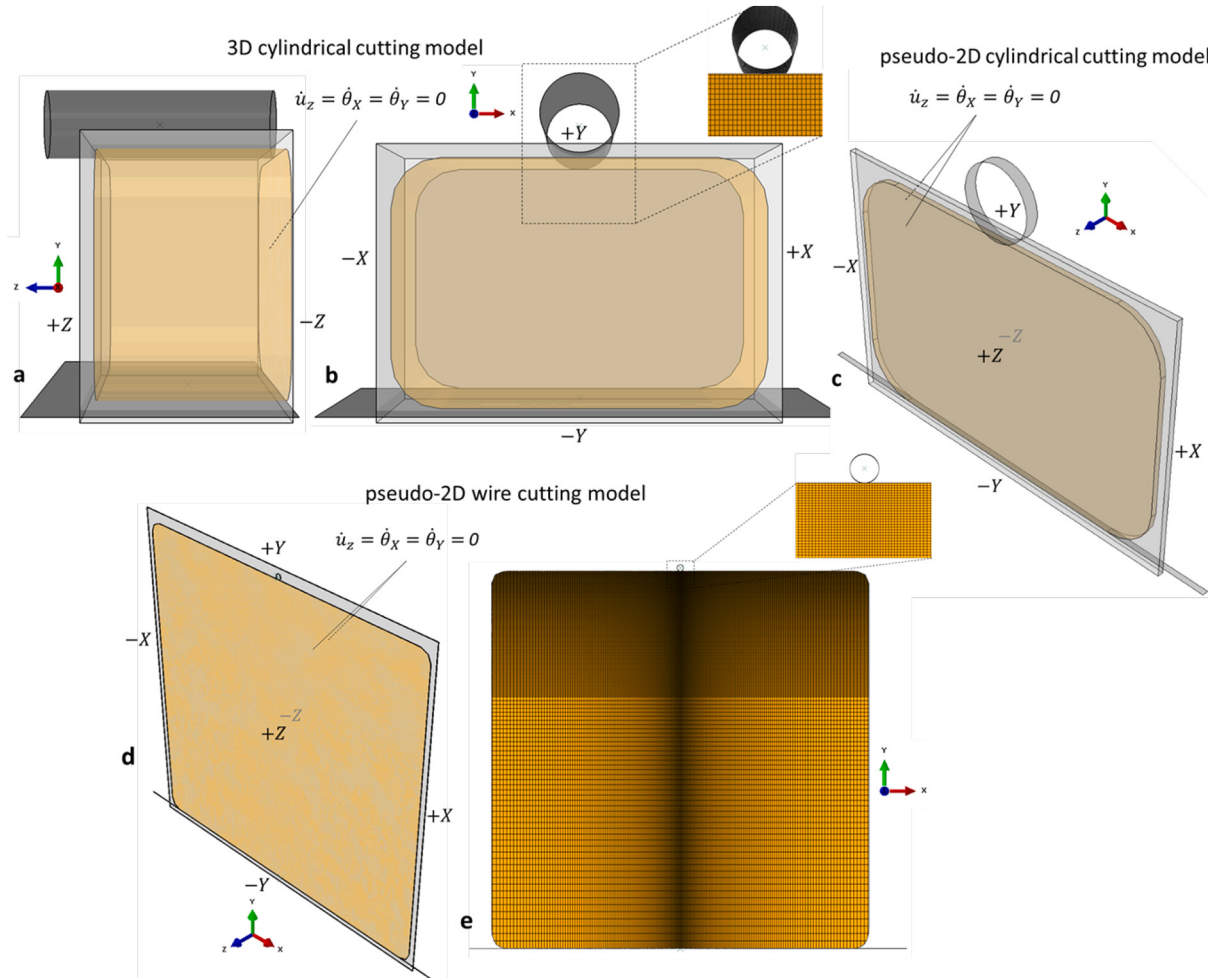


**Fig. 2.** Illustration of cutting models. Images show: (a) side view, (b) front view with mesh details at the cutting region of the 3D cylindrical cutting model; (c) shows pseudo-2D cylindrical cutting model. (d) shows pseudo-2D wire cutting model, and (e) shows corresponding Eulerian mesh for wire cutting specimen together with mesh details at the wire cutting region.

were generally allowed until an element aspect ratio of 1.5 was reached, while domain translation was such that the ‘negative’ bounding faces in the Y, Z axes (denoted as  $-Y$ ,  $-Z$  in Figs. 2(a-b)) remain fixed; in the pseudo-2D models (Figs. 2(c-d)) the  $+Z$  face were

also fixed. In all models the rigid parts were discretised by 4-node, bilinear rigid quadrilateral elements with uniform size 0.5 mm, while the Eulerian domain was meshed via 8-node, linear, Eulerian brick, reduced integration, hourglass controlled elements. The Eulerian mesh

### Construction of FE gastric model

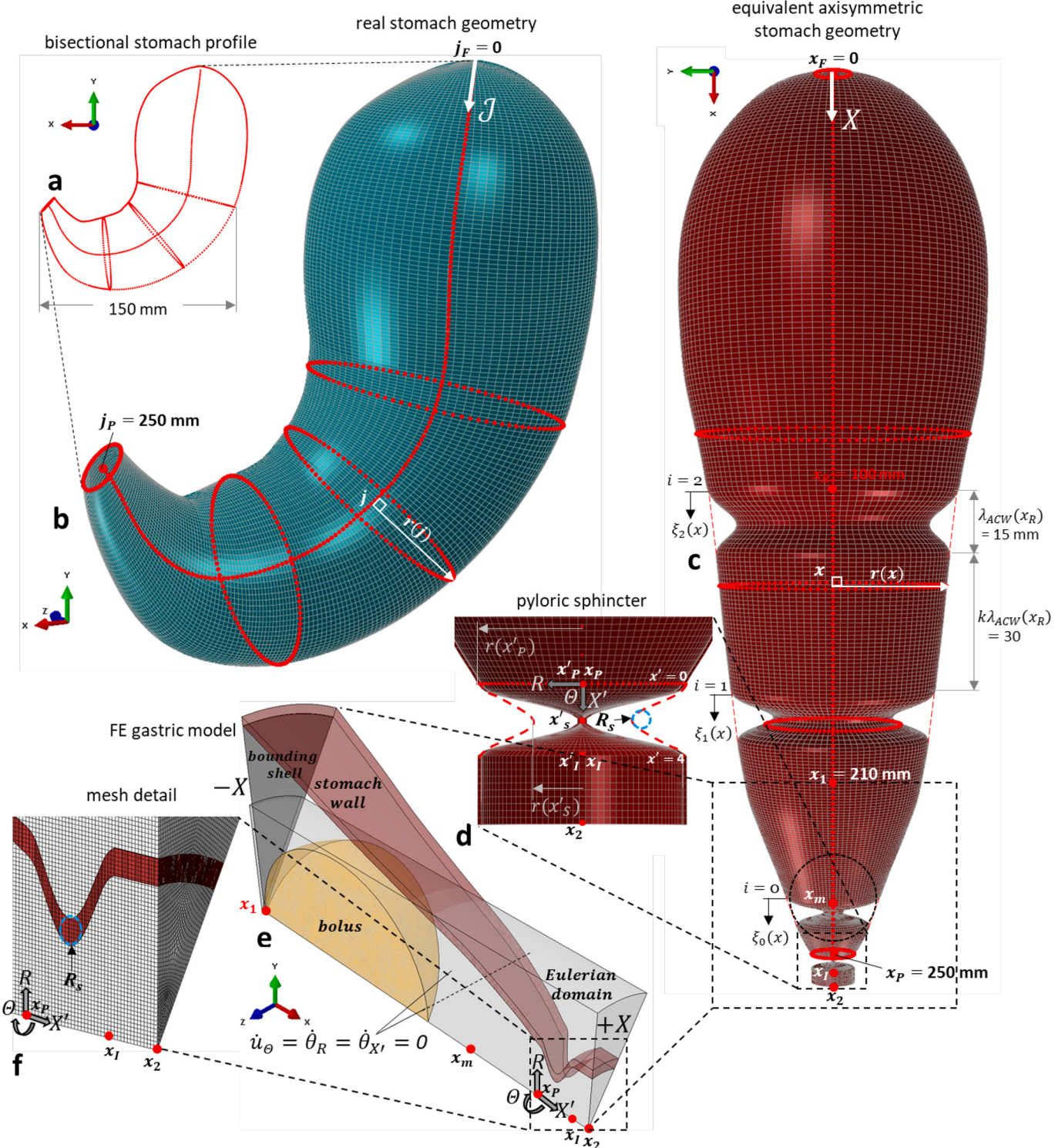


**Fig. 3.** Illustration of the construction of the gastric FE model. Images show: (a) stomach cross sectional profile in X-Y plane reconstructed via Image J from (Ferrua & Singh, 2010), (b) 3D mesh of shell geometry reconstructed from the profile shown in (a) with curved axis/line of symmetry,  $J$ , ( $j$  are curvilinear coordinates) (c) equivalent stomach configuration with straight axis/line symmetry,  $X$ ; three ACWs are applied based on displacement function in Eq. (15). (d) shows detail of the pylorus-sphincter geometry, and (e) shows final gastric FE Eulerian model assembly corresponding to a 30° segment of the real geometry shown in (c) and including only the region  $x_1 \leq x \leq x_2$ ; axisymmetric boundary conditions are also denoted. Finally, (f) depicts the detail of the FE model in the pylorus-sphincter region.

was chosen such that the cutting force-displacement results do not change significantly with mesh refinement i.e. a converged solution is obtained. Preliminary simulations in both wire and cylindrical cutting indicated that the above condition is reached even when the Eulerian element size/length at the cutting region is as large as 12% of the cutting size/diameter. Therefore, a uniform element size of 0.5 mm

(10% of  $d_c = 5$  mm) throughout the entire domain was used for cylindrical cutting, leading to Eulerian meshes of 113,720 elements and 5415 elements in the 3D (Fig. 2(a-b)) and pseudo-2D (Fig. 2(c)) models, respectively. Instead, as illustrated in Fig. 2(e) mesh bias is used in the wire cutting model, such that the mesh density maximises in the wire cutting region; for this region, the minimum element size is 0.05 mm

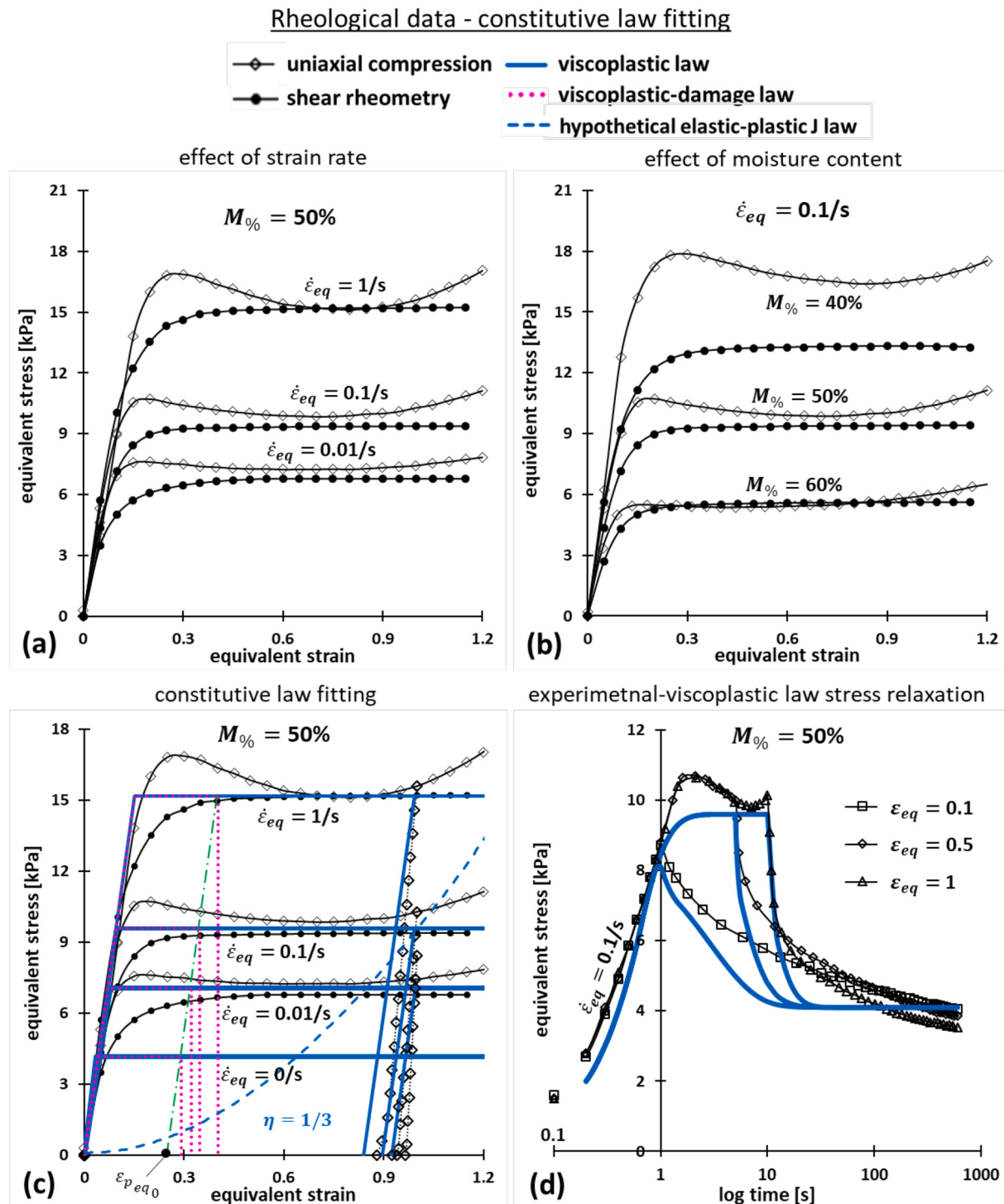


**Fig. 4.** Summary of rheological test  $\sigma_{eq} - \epsilon_{eq}$  results together with viscoplastic law fit. Plots show: (a) monotonic uniaxial compression  $\sigma_{eq} - \epsilon_{eq}$  data in comparison to shear rheometry data for fixed moisture content,  $M\% = 50\%$ , and three strain rates,  $\dot{\epsilon}_{eq} = 0.1/s$ ,  $0.01/s$ ,  $\dot{\epsilon}_{eq} = 1/s$ , (b) comparison between compression and shear rheometry data for fixed rate,  $\dot{\epsilon}_{eq} = 0.1/s$ , and moisture content varying between  $M\% = 40\%$ ,  $M\% = 50\%$  and  $M\% = 60\%$ . (c) viscoplastic law fit (solid blue line) on monotonic compression and rheometry data for  $M\% = 50\%$ , including response when unloading from  $\epsilon_{eq} = 1$  at three rates, as well as viscoplastic-damage law response (pink dotted lines) in tension ( $\eta = 1/3$ ) for damage onset strain,  $\epsilon_{peq0} = 0.25$ , highlighted by green dashed line; the hypothetical elastic-plastic J law response is also plotted (blue dashed line). (d) viscoplastic law fit on relaxation (compression,  $M\% = 50\%$ ) at three strain levels,  $\epsilon_{eq} = 0.1$ ,  $\epsilon_{eq} = 0.5$  and  $\epsilon_{eq} = 1$ .

(10% of  $d_w = 0.5$  mm). A total of 45,254 elements was used in the model of Fig. 2(e).

#### 2.4.5. Gastric model

**2.4.5.1. Construction and main considerations of gastric model.** Our gastric model builds upon the geometry presented by Ferrua et al (Ferrua & Singh, 2010) and specifically the cross sectional profile of the stomach at its bisectional  $X - Y$  plane, shown in Fig. 3(a). The profile was used to generate  $x, y$  coordinates corresponding to the perimeter and curved axis/line of symmetry,  $\mathcal{J}$ , within the Image J software, which were then imported in Solid Works (Documentation, 2010) to construct the 3D shell geometry illustrated in Fig. 3(b). The latter was then imported in ABAQUS CAE (Simulia, 2013) to perform meshing.

Due to the unknown effect of a number of parameters in the mechanics of gastric bolus breakdown e.g. bolus mechanical properties, surrounding liquid flow patterns, gravity, bolus-stomach wall interaction properties, stomach fill ratio, the following three assumptions were adopted:

- (i) zero gravity,
- (ii) absence of liquid environment,
- (iii) symmetry about the middle plane  $X - Y$  (see Fig. 3(b)).

Assumption (i) implies that bolus acceleration is only driven by ACWs, whereas assumption (ii) implies that the entire bolus response, including rigid body displacements-accelerations and deformation-fracture patterns, is not influenced by the surrounding flow of gastric liquids (chyme). On the other hand, assumption (iii) allows for modelling half of the model assembly; nevertheless, the model is here simplified and reduced in size in a different manner. In particular, based on no gravity and liquid environment, it was reasonable to hypothesise that the curvature of the gastric geometry (Fig. 3(b)) will not play an important role in the bolus deformation-fracture results. The model predictions are thus not expected to change considerably if ACWs are applied within an alternative stomach configuration of the same size but of a different shape. As a result, the original (curved) geometry (Fig. 3(b)) was converted into its ‘equivalent’ axisymmetric configuration without curvature i.e. straight axis/line of symmetry,  $X$  (with origin  $x = x_F = 0$ , where ' $F$ ' denotes the gastric fundus) illustrated in Fig. 3(c); a similar approach was recently used by Alokaily et al. (Alokaily et al., 2019). The added geometries of pyloric sphincter (between points,  $x_P = 250$  mm and  $x_I = 254$  mm in Fig. 3(d), where ‘ $P$ ’ and ‘ $I$ ’ respectively denote the beginning and the end of gastric pylorus), and the beginning of small intestine (between points,  $x_I = 254$  mm and  $x_2 = 256$  mm in Fig. 3(d)) will be described in Section 2.3.5.2. Equivalency between the configurations in Figs. 3(b) and 3(c) here implies: common total length of 250 mm for lines  $\mathcal{J}$  and  $X$ , defined by the corresponding end point coordinates,  $j_F = 0$ ,  $j_P = 250$  mm, and  $x_F = 0$ ,  $x_P = 250$  mm, respectively, as well as common gastric wall radius i.e.  $r(j) = r(x)$ , for any pair of  $j$  and  $x$  coordinates that refer to the same relative position along the axes lines  $\mathcal{J}$  and  $X$ ; note that  $j$  are curvilinear coordinates. As a consequence of the above, the two geometries (Figs. 3(b-c)) also enclose the same volume of 0.88 L, close to the 0.9 L used by Ferrua et al. (Ferrua & Singh, 2010).

Eventually, the simplified geometry (Fig. 3(c)) combined with the absence of gravity gives rise to the hypothesis of general axisymmetry with respect to the  $X$  axis. This was modelled by using a 30° segment of the actual assembly (De Cock, Massinon, Mercatoris, & Lebeau, 2014), leading to the final gastric model depicted in Fig. 3(e); note that the latter includes only the region between points  $x_1 = 210$  mm and  $x_2 = 256$  mm out of the entire geometry shown in Fig. 3(c) (cropped region  $x_1 < x < x_2$  is denoted by the dashed black box). This allowed us to focus on the most critical phenomena taking place in the antrum-pyloric region (Alokaily et al., 2019) whilst also reducing the computational cost; the antrum-pyloric region involves the most severe mechanical loading due to the large occlusion of the ACWs, from one side,

and the constriction by the sphincter from the other (Alokaily et al., 2019; Ferrua & Singh, 2010). The choice of exact coordinate,  $x_1 = 210$  mm, at which the model in Fig. 3(c) is cropped to give the model in Fig. 3(e) was arbitrary.

**2.4.5.2. Computational aspects of gastric model.** The gastric model (Fig. 3(e)) consists of a deformable (Lagrangian) gastric wall of 1 mm thickness and total length of 46 mm along the  $X$ -axis (between points  $x_1 = 210$  mm and  $x_2 = 256$  mm), a wedge shaped Eulerian domain of 46.5 mm length and radius  $\approx 13.5$  mm within which a segment of the Eulerian spherical bolus is contained, and a discrete rigid (Lagrangian) bounding shell which prevents bolus material outflow from the Eulerian domain in the backward direction i.e. at the  $-X$  face of the domain; the bounding shell overlaps with the Eulerian domain. A bolus radius of 12.8 mm was used (mass 9.8 g), such that the corresponding volume of 8.8 mL is 1% of the total gastric volume (dashed circle in Fig. 3(c)). Based on previous work by Bornhorst et al. (Bornhorst & Singh, 2013) and Prinz et al. (Prinz & Heath, 2000), the radius 12.8 mm represents a realistic bolus size. The radius  $\approx 13.5$  mm of the Eulerian domain was chosen large enough such that the enclosed Eulerian bolus material never approaches the free boundary of the domain i.e. the curved face normal to the radial,  $R$ , direction (see local coordinate system,  $R\theta X'$ , in Fig. 3(e)). This ensures that bolus material outflow does not occur from the domain; note that this required some a-priori knowledge of the flow-breakdown patterns by performing preliminary simulations. Simultaneously, the Eulerian domain was chosen small enough in order to reduce computational cost. On the other hand, Fig. 4e shows that in the original model configuration, the Lagrangian (deformable) gastric wall overlaps partially with Eulerian domain, with a large fraction of the wall initially lying outside of the domain. This detail does not play a role in the simulations here, since when the gastric wall deforms i.e. by the application of antral contraction waves (ACWs), any gastric wall-bolus contact occurs within the Eulerian domain. A 1 mm thickness was chosen for the Lagrangian gastric wall such that the latter occupies space equivalent to at least three elements of the overlapping Eulerian domain; this is essential in preventing the unphysical numerical phenomenon of Eulerian bolus material escaping through the Lagrangian gastric wall. This erroneous phenomenon can initiate by the typical numerical effect called ‘Eulerian-Lagrangian contact penetration’ (Simulia, 2013) (Eulerian bolus penetration onto the Lagrangian wall), which can become pronounced here when the bolus undergoes large hydrostatic compressive states (very low stress triaxialities e.g.  $\eta < -10$ ); as it will be shown in Section 3.3, these states can occur when the bolus is compressed between a contraction wave and a closed pylorus. Bolus-stomach friction coefficient, and the ratio of bulk moduli between the bolus material and the gastric wall are additional parameters that can influence the degree of the above bolus-gastric wall penetration phenomenon. In our simulations, we ensure that Eulerian-Lagrangian penetrations are small and that the bolus material does not escape through the gastric wall. To reduce further the computational cost, the end point coordinate,  $x_2 = 256$  mm of the Eulerian domain was chosen to be only slightly larger than  $x_I = 254$  mm, such that the number of elements corresponding to the regime of no interest,  $x_I > 254$  mm, is minimised. The boundary conditions were applied with respect to the local coordinate system,  $R\theta X'$  (see Fig. 3(e)), mounted at the beginning of the pylorus i.e. point  $P$  ( $x'_P = 0$ ); these include: fixed rigid bounding shell as well as axisymmetric conditions of zero normal velocity,  $u_\theta = 0$ , in the  $\theta$  direction and zero rotational velocities,  $\dot{\theta}_R = \dot{\theta}_{X'} = 0$ , about  $R, X'$  axes (see Fig. 3(e)).

A total of 13,806 8-node, linear, brick, reduced integration, hourglass control elements (typical element size 0.1 mm) were used to mesh the gastric wall, while using a single element through the thickness. A 1 mm thickness was chosen such that the gastric wall occupies space equivalent to at least three elements of the Eulerian domain, which is essential in preventing Eulerian-Lagrangian contact penetration.

Instead, the Eulerian mesh density was chosen based on the preliminary mesh convergence results from cylindrical and wire cutting; these indicated converged solutions for Eulerian elements sizes up to 12% the diameter of the cutter (Section 2.4.4). Therefore, in the gastric model, by considering the tip of the undeformed/open pyloric sphincter as a cutter with an approximate local radius of curvature,  $R_s = 0.6$  mm (denoted by blue dashed circles in Figs. 3(d), 3(f)), it was assumed that a uniform Eulerian element size of 0.15 mm ( $\sim 12\%$  of  $2R_s = 1.2$  mm) also leads to converged solutions; note that the gastric geometry and motility patterns will be chosen such that practically the same local radius of curvature,  $R_s = 0.6$  mm, characterises the tip of the pyloric sphincter (Figs. 3(d), 3(f)) and the tip of ACWs. The element size of 0.15 mm here leads to a mesh size of 894,350 8-node, linear, Eulerian brick, reduced integration, hourglass control elements. Due to the considerable computational cost of the simulations, mesh dependency was not studied here. The high computational cost partially owes to the large mesh size, but more significantly, it is induced by the requirement for an ACW speed of 2.5 mm/s which here results into a simulated total gastric processing time duration,  $\Delta t = 32$  s. The latter was extremely long to simulate through an Explicit FE integration i.e. requires millions of calculation increments (Benson, 2000). The duration of  $\Delta t = 32$  s was calculated based on the number of subsequent ACWs applied (here two ACWs are applied), the distance between them, as well as the total ACW travel distance i.e. here 46 mm length between  $x_1 = 210$  mm and  $x_2 = 256$  mm.

Four gastric processing cases are simulated, as outlined below:

**case A.** viscoplastic-damage law and stomach-bolus friction coefficient,  $\mu = 0.9$ ,

**case B.** viscoplastic-damage law and frictionless stomach-bolus contact,

**case C.** viscoplastic law (no damage) and stomach-bolus friction coefficient,  $\mu = 0.9$ ,

**case D.** hypothetical elastic-plastic J law and stomach-bolus friction coefficient,  $\mu = 0.9$ .

The FE contours associated with these scenarios will be presented in Fig. 8.

#### 2.4.5.3. Gastric motility

**2.4.5.3.1. Pyloric sphincter geometry.** In contrast to Ferrua et al. (Drechsler & Ferrua, 2016) and other related in-silico studies (Alokaily et al., 2019; Imai et al., 2013; Kozu et al., 2010), the assumption of a closed pylorus was not adopted here. Instead, we considered the original pyloric sphincter geometry shown in Fig. 3(e), which can close and re-open. Fig. 3(d) shows the details of pyloric sphincter geometry at the closed state, with the red dashed line representing the open state. Based on the local coordinate system,  $R\theta X'$ , mounted at point  $P$  i.e.  $x'_P = 0$  (for which  $x_P = 250$  mm based on global system,  $XYZ$ ), the original/open sphincter configuration (denoted by red dashed line in Fig. 3(d) – corresponding tip radius of curvature,  $R_s = 0.6$  mm, is denoted by blue dashed circle) can be described by the following customised function of the original radial coordinates,  $r$ , of the inner nodes of the pyloric sphincter wall:

$$r(x') = r(x'_P) \left\{ 1 - C_{s1} [x'(\lambda_s - x')]^{a_s} \left( \frac{\lambda_s}{2} \right)^{-2a_s} \right\} \quad (12)$$

where the local position,  $x'$ , lies within  $x'_P = 0 \leq x' \leq x'_I = 4$ ,  $r(x'_P) = 6$  mm denotes the original radial coordinates of the inner nodes at the beginning of the pylorus (point  $P$ ),  $C_{s1} = 0.75$  (–/–) is the relative occlusion of the original/open sphincter, giving rise to a sphincter opening radius  $r(x'_s) = 1.5$  mm,  $a_s = 2$  (–/–) is a shape parameter controlling the sharpness of sphincter, and  $\lambda_s = 4$  mm is the sphincter width (similar to the concept of wavelength), such that  $x'_s - \frac{\lambda_s}{2} = x'_P$  and  $x'_s + \frac{\lambda_s}{2} = x'_I$ . The values  $r(x'_s)$  and  $\lambda_s$  were chosen to agree with

dimensions reported in the literature (Keet Jr. 1962; Ferrua & Singh, 2010). Beyond point  $x'_I$  (represents beginning of the small intestine), bolus flow-breakdown was not investigated and a constant profile is assumed i.e.  $r(x) = 6$  mm for  $x > x_I$  (see Fig. 3(d)).

**2.4.5.3.2. Pyloric sphincter opening-closing.** Sphincter closing was applied with respect to the local system,  $R\theta X'$ , by prescribing in all the nodes lying within  $x'_P = 0 \leq x \leq x'_I = 4$  the below radial displacements,  $dr$ :

$$dr(x', t) = -\dot{C}_s t r(x'_s) [x'(\lambda_s - x')]^{a_s} \left( \frac{\lambda_s}{2} \right)^{-2a_s} \quad (13)$$

A rate of  $\dot{C}_s = 10/\text{s}$  was used such that full closure is completed within 0.1 s. Thereafter, the sphincter remained closed by keeping  $dr(x', t)$  constant i.e. using  $\dot{C}_s t = 1$  in Eq. (13), while sphincter re-opening was applied by using a negative occlusion rate,  $\dot{C}_s = -10/\text{s}$  in Eq. (13). The above patterns, including the ACWs described next, are prescribed through the ABAQUS user defined displacement subroutine, *VDISP* (Simulia, 2013).

**2.4.5.3.3. Implementation of ACWs.** For clarity, this section firstly describes the mathematical implementation of ACWs for the general case of the three subsequent ACWs ( $i = 0, 1, 2$ ) shown in Fig. 3(c) (case not used in final gastric simulations). Thereafter, using the same methodology, the more complex motility patterns were applied in the reduced gastric model to predict bolus flow-breakdown are described in Section 2.3.5.3.4. The three ACWs illustrated in Fig. 3(c) initiate from an arbitrary point,  $x_R = 100$  mm, and each of them corresponds to a local position function,  $\xi_i(x)$  (mm), defined as:

$$\xi_i(x) = x - x_R + (ik + 1)\lambda_{ACW}(x_R) - \dot{x}_{ACW}t \quad (14)$$

where  $i = 0, 1, 2$  is a counting number assigned to each newly generated ACW, in time order, for the total of three generated ACWs (see Fig. 3(c)), and  $k$  (–/–) defines the distance between subsequent ACWs in multiples of  $\lambda_{ACW}(x_R)$  (mm), which is the initial ACW width/wavelength at the point where ACWs originate i.e. point  $x_R$ . The equation for the radial displacements,  $dr(x, t)$ , associated with ACWs is deduced by substituting the terms  $x'$ ,  $a_s$ ,  $\lambda_s$ ,  $r(x'_s)$  and  $\dot{C}_s t$  in Eq. (13), with the corresponding terms  $\xi_i(x)$ ,  $a$ ,  $\lambda_{ACW}(x)$ ,  $r(x)$  and  $C_{ACW}(x)$ , leading to:

$$dr(x, t) = -C_{ACW}(x)r(x)\{\xi_i(x)[\lambda_{ACW}(x) - \xi_i(x)]\}^a \left[ \frac{\lambda_{ACW}(x)}{2} \right]^{-2a} \quad (15)$$

where  $a = 5$  (–/–) is the shape parameter that controls the sharpness of ACWs,  $\lambda_{ACW}(x)$  (mm) is the ACW width/wavelength prescribed as a function of position,  $x$ ,  $r(x)$  (mm) is the original radial coordinates of the nodes of the gastric wall and  $C_{ACW}(x)$  (–/–) is the ACWs relative occlusion also prescribed as a function of position,  $x$ . Importantly, Eq. (15) was applied only for nodes with  $x$  coordinates satisfying:  $x - \xi_i(x) \leq x \leq x - \xi_i(x) + \lambda_{ACW}(x_R)$ ; when this condition is not met,  $dr(x, t) = 0$  is applied instead of Eq. (15) which refers to the undeformed regions of the gastric wall lying between subsequent ACWs e.g. in Fig. 3(c) an undeformed region of length,  $k\lambda_{ACW}(x_R) = 30$  mm, was prescribed by using  $k = 2$  (–/–) and  $\lambda_{ACW}(x_R) = 15$  mm. In all the nodes of the gastric geometry, all the degrees of freedom except for radial translation, were constantly constrained to zero. From a physical perspective, the value of the parameter,  $a = 5$  (–/–), was chosen such that it leads to realistic ACW geometries similar to the corresponding geometries presented in (Berry et al., 2016; Ferrua & Singh, 2010); note that geometric parameters other than width/wavelength for ACWs have not been reported before in the open literature. From a numerical perspective, the  $a$  parameter must be small enough to avoid ACWs with an extremely sharp tip, which would otherwise cause severe element distortion in the Lagrangian gastric wall.

**2.4.5.3.4. Applied gastric motility patterns.** In order to apply ACWs in the reduced gastric model (Fig. 3(e)), we considered that ACWs initiate at point,  $x_1$ , instead of  $x_R$ . Therefore, in this case Eqs. (14–15) were used in the same manner with the only difference that  $x_R$  is replaced with  $x_1$ .

The gastric motility patterns will be illustrated in Fig. 8, together with the food flow-breakdown results. The following idealisation was adopted: two subsequent ACWs initiate at point,  $x_1$ , ( $i = 0, 1$  used in Eq. (14)) and travel with constant velocity  $\dot{x}_{ACW} = 2.5$  mm/s, while their width/wavelength is set to decrease linearly from the initial value,  $\lambda_{ACW}(x_1) = 20$  mm, at point  $x_1$ , down to  $\lambda_{ACW}(x_p) = 10$  mm, at point  $x_p$  (compare wavelength between 1st and 2nd ACW for time  $t = 14$  s in Fig. 8) and thereafter remain constant i.e. for  $x > x_p$ . The distance between the two ACWs was arbitrarily chosen equal to  $k\lambda_{ACW}(x_1) = 36$  mm ( $k = 1.2$  used in Eq. (14)). Both the first and second ACW increase their relative occlusion linearly from zero (at point  $x_1$ ) up to  $C_{ACW}(x_m) = 0.9$  at a point,  $x_m$ , (again compare 1st and 2nd ACW for time  $t = 14$  s in Fig. 8) which was here arbitrarily chosen to be at distance 10 mm from the pylorus (see Figs. 3(c), 3(e); instead, the values  $C_{ACW}(x_m)$ ,  $\lambda_{ACW}(x_1)$ ,  $\lambda_{ACW}(x_p)$  and  $\dot{x}_w$  were based on in-vivo gastric motility data (Kwiatek et al., 2006). As soon as the first ACW reaches point  $x_m$ , the sphincter closes and the ACW relative contraction starts decreasing such that it becomes zero after 5 mm of further propagation i.e. at the coordinate,  $x = x_m + 5$  mm (see Fig. 8 for time  $t = 18$  s). When the second ACW reaches  $x_m$ , the sphincter re-opens i.e. according to Eq. (13) for  $\dot{C}_s = -10/\text{s}$  (see Fig. 8 for time  $t = 22.5$  s), and then deforms as the ACW propagates through it i.e. according to Eq. (15) (see Fig. 8 for time  $t = 29$  s). This implies that the second ACW retains its relative occlusion at 0.9 until the end point,  $x_2$ .

### 3. Results and discussion

#### 3.1. Stress-strain results

##### 3.1.1. Rheological data

In the rheological data, the maximum error between test repeats occurred when  $\dot{\varepsilon}_{eq} = 1/\text{s}$  and  $M\% = 40\%$  and corresponded to 6.5% and 8.2% variation in the average plateau stress value, calculated within  $0.3 < \dot{\varepsilon}_{eq} < 1$ , for the compression and shear rheometry tests, respectively. Fig. 4(a) shows a close overall agreement between the uniaxial compression and shear rheometry  $\sigma_{eq} - \varepsilon_{eq}$  data, for the moisture content,  $M\% = 50\%$  and three rates,  $\dot{\varepsilon}_{eq}$ : 0.01/s, 0.1/s and 1/s, adding credibility to the experimental methodology. The agreement between the two tests is however shown to breakdown in Fig. 4(b) (for  $\dot{\varepsilon}_{eq} = 0.1/\text{s}$ ) when  $M\% = 40\%$ ; the same was found for  $\dot{\varepsilon}_{eq} = 0.01/\text{s}$  and  $\dot{\varepsilon}_{eq} = 1/\text{s}$  (data not shown) and it is mainly attributed to specimen-platen slippage effects in the shear rheometry test (Iqbal et al., 2020), both being profound at low  $M\%$ .

Both compression and shear rheometry display a typical elastic-rate dependent perfectly plastic  $\sigma_{eq} - \varepsilon_{eq}$  response (referred here as

viscoplastic). The slight decrease in  $\sigma_{eq}$  in the regime  $0.1 < \dot{\varepsilon}_{eq} < 1$  in compression, particularly for increasing  $\dot{\varepsilon}_{eq}$ , is attributed to lubricant being squeezed out of the specimen-platen interface with increasing testing speed i.e. increasing  $\dot{\varepsilon}_{eq}$  (Skamniotis et al., 2017). The compression data are considered valid up to  $\varepsilon_{eq} = 1$  and for  $\varepsilon_{eq} > 1$  the true stress-strain behaviour is assumed to remain perfectly plastic i.e. constant  $\sigma_{eq}$ . This is because beyond  $\varepsilon_{eq} = 1$  inevitable specimen barrelling and circumferential micro-cracking (see Fig. 1c) effects were observed; such effects have been previously shown to violate the uniformity of applied strains, which implies that the  $\sigma_{eq} - \varepsilon_{eq}$  data are no longer specimen geometry independent (Charalambides et al., 2005; Skamniotis et al., 2017; Skamniotis and Charalambides, 2020). On the other hand, the shear rheometry  $\sigma_{eq} - \varepsilon_{eq}$  data are found practically independent of: (a) gap size, (b) level of material pre-straining, as well as (c) material relaxation time prior to the tests (results not shown). Condition (b) implies that no damage mechanism is involved when the material is squeezed between the plates prior to shearing. Instead, condition (c) highlights that the measured torque based on which the  $\sigma_{eq} - \varepsilon_{eq}$  data are deduced, is independent of the normal force applied on the specimen at the onset of shearing i.e. at the beginning of test; note that this force decreases with relaxation time (Iqbal et al., 2020).

Regarding specimen damage effects, these were not observed when  $M\% = 60\%$  at any strain level in both compression-shear rheometry tests. Instead, when  $M\% = 50\%$  signs of edge fracture (Iqbal et al., 2020) can be appreciated in Fig. 1(d), at the strain,  $\gamma = 0.8$  (corresponding to  $\dot{\varepsilon}_{eq} = 0.47$ ), for shear rheometry, as well as micro-cracking in Fig. 1c for compression. The above damage effects in both tests were observed to occur at lower applied strains when  $M\% = 40\%$ , reasonably indicating that the material cohesiveness degrades with a dry content i.e. decreasing  $M\%$ . Interestingly, however, these damage effects here do not lead to an obvious decrease in  $\sigma_{eq}$  in the regime  $\varepsilon_{eq} > 0.2$  for both tests in Figs. 4(a-b). Only a slight gradual decrease of  $\sigma_{eq}$  was observed in the shear rheometry data approximately for  $\varepsilon_{eq} > 1$ , due to the initiation of specimen-plate slippage effects (data not shown). Indeed, it was observed that the originally vertical line depicted in Fig. 1(f), started being gradually disjointed at the specimen-platen interfaces approximately beyond  $\varepsilon_{eq} = 0.7$  for  $M\% = 50\%$ , and beyond  $\varepsilon_{eq} = 0.45$  for  $M\% = 40\%$ . The latter explains the discrepancy shown for  $M\% = 40\%$  between the compression and shear rheometry in Fig. 4(b), and lends weight to uniaxial compression as a more reliable test for determining the solid bolus response at large strains.

##### 3.1.2. Constitutive law fitting

As shown by Figs. 4(c-d), the  $\sigma_{eq} - \varepsilon_{eq}$  response of the oatcake bolus here is accurately captured by the viscoplastic law (see solid blue lines);

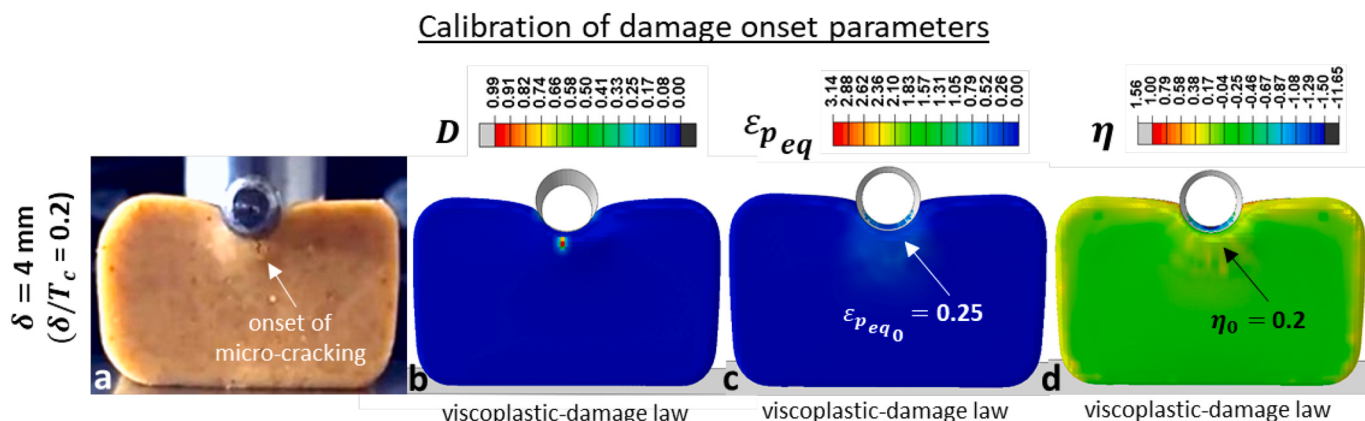


**Fig. 5.** Illustration of the inverse calibration of damage onset parameters,  $\varepsilon_{peq}$  and  $\eta_0$  for the viscoplastic-damage law based on the initiation of micro-cracking in the cylindrical cutting test. Images show: (a) experimental specimen behaviour at displacement  $\delta = 4$  mm (when micro-cracking initiates), (b) corresponding FE predictions ( $D$  contours) for viscoplastic-damage law with calibrated parameters,  $\varepsilon_{peq0} = 0.25$  and  $\eta_0 = 0.2$ , (c) corresponding  $\varepsilon_{peq}$  contours, and (d) corresponding  $\eta$  contours.

this is particularly true for the monotonic and unloading curves (Fig. 4(c)), while the relaxation curve (Fig. 4(d)) is less accurately reproduced due to the absence of a time dependent strain component i.e. viscous strain, in the currently used viscoplastic law (Skamniotis et al., 2018). Specifically, the response is idealised in the form of an initially linear elastic regime with  $E = 100$  kPa, followed by a rate dependent, perfectly plastic regime, such that  $\sigma_{eq}$  is constant beyond the onset of plasticity for each rate, and takes values 4.1 kPa, 7 kPa, 9.6 kPa, 15.2 kPa, for 0/s, 0.01/s, 0.1/s, 1/s, respectively; the rate  $\dot{\epsilon}_{eq} = 0/s$  represents the static response and is chosen to correspond to the long term stress 4.1 kPa measured at ten minutes relaxation (Skamniotis et al., 2018). The unloading curves (Fig. 4(c)) highlight that the bolus exhibits little elastic recovery with the unloading strain (at  $\sigma_{eq} = 0$ ) being fully plastic/permanent; this is because practically no further viscoelastic recovery was observed when the loading platen was removed from the specimen, even after the elapse of ten minutes; the same was found when unloading from smaller strains i.e.  $\epsilon_{eq} = 0.5$  (data not shown). Fig. 4(c) also includes the response of the hypothetical elastic-plastic J law (see dashed blue line) based on the calibrated parameters,  $\sigma_{eqch} = 20$  kPa,  $\epsilon_{eqch} = 1.5$ ,  $m = 2$  and  $A = 11.78$  kPa, (and  $E = 100$  kPa) as well as the response of the coupled viscoplastic-damage law (see pink dotted lines) based on the damage parameters,  $\epsilon_{peq0} = 0.25$ , and  $\eta_0 = 0.2$ , calibrated inversely via the cylindrical cutting test (to be described in Section 3.2.3); the damage onset value,  $\epsilon_{peq0} = 0.25$ , is highlighted in Fig. 4(c) through the green dashed line. The wire-cylindrical cutting FE predictions and flow breakdown FE predictions obtained for each of the constitutive laws illustrated in Fig. 4(c) i.e. viscoplastic law, viscoplastic-damage law and hypothetical elastic-plastic J law, will be presented and discussed in Sections 3.2.3 and 3.3.3, respectively.

### 3.2. Cutting results

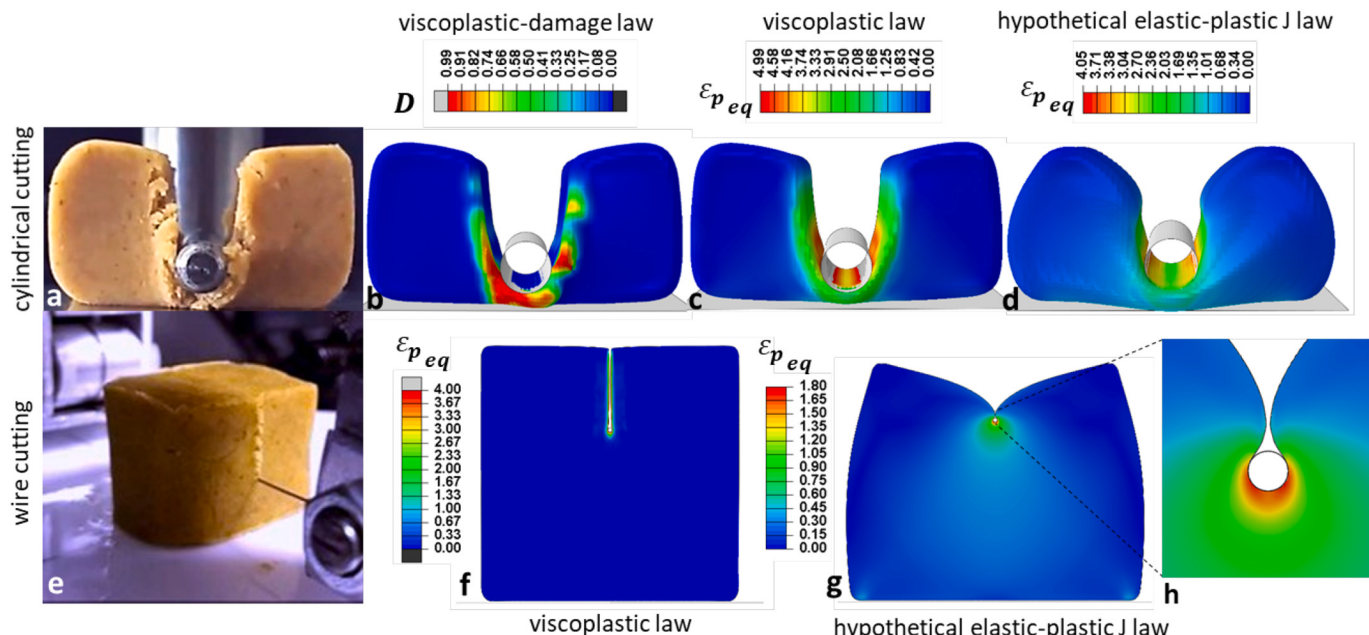
#### 3.2.1. Experimental cutting data

Fig. 5(a) shows the specimen behaviour at cylindrical cutting

displacement,  $\delta = 4$  mm; at t surface micro-cracking typically initiates near the indentation region. For the same  $\delta = 4$  mm, Figs. 5(b), 5(c) and 5(d) respectively show the damage variable,  $D$ , equivalent plastic strain,  $\epsilon_{peq}$ , and stress triaxiality,  $\eta$ , FE contours predicted via the viscoplastic-damage law for the damage onset parameters,  $\epsilon_{peq0} = 0.25$  and  $\eta_0 = 0.2$ ; these parameters are calibrated such that the first damage onset in the model i.e. in Fig. 5(b), occurs at the same cutting displacement,  $\delta = 4$  mm, as in the experiment. Figs. 6(a) and 6(e) illustrate typical specimen behaviour during cylindrical cutting and wire cutting, at displacements,  $\delta = 20$  mm and  $\delta = 10$  mm, respectively. The corresponding normalised cutting force,  $F/T_c d_c$  ( $F/T_w d_w$  for wire cutting) versus normalised displacement,  $\delta/H_c$  ( $\delta/H_w$  for wire cutting) data are provided in Figs. 7(a) and 7(b), for cylindrical and wire cutting, respectively, together with the FE model predictions based on the viscoplastic law. Forces are normalised over the product of specimen thickness,  $T_c$  ( $T_w$  for wire cutting) and cutting diameter,  $d_c$  ( $d_w$  for wire cutting), and displacements are normalised over the specimen height,  $H_c$  ( $H_w$  for wire cutting), to enable comparison between the cylindrical and wire cutting normalised force data. A maximum variation of 7% and 5% is found in the average steady state experimental force values over the three repeats, amongst all speeds, in wire cutting and cylindrical cutting, correspondingly. Both Figs. 7(a-b) highlight strong time dependency in the experimental cutting forces, attributed to the strong rate dependent  $\sigma_{eq} - \epsilon_{eq}$  response of the oatcake bolus. However, the shape of the plots between cylindrical and wire cutting is different. This is because large deformations and damage (micro-cracking) occur within a very small volume of the specimen in wire cutting (see Fig. 6(e)), as opposed to cylindrical cutting where such processes occupy a considerable portion of the specimen (see Figs. 6(a)). As a result, a steady state force exists in the wire cutting test for  $\delta/H_w > 0.05$ , whereas it does not exist in the cylindrical cutting test where the force continues to rise with displacement.

In both tests, large plastic strains and damage occur only locally in the cutting region such that the rest of the specimen exhibits very little

### Experimental-model cutting FE contours: effect of constitutive law



**Fig. 6.** Illustration of experimental-FE specimen behaviour during cutting. Images show: (a) typical specimen behaviour in cylindrical cutting experiment at maximum displacement,  $\delta_{max} = 18$  mm, (b) corresponding FE predictions ( $D$  contours) based on the viscoplastic-damage law, (c) based on the viscoplastic law (no damage), and (d) based on the hypothetical elastic-plastic law; images (b-c) show  $\epsilon_{peq}$  contours. For wire cutting, image (e) shows typical specimen behaviour at experimental displacement,  $\delta = 20$  mm, while images (f-g) show corresponding FE predictions ( $\epsilon_{peq}$  contours) based on the viscoplastic and hypothetical elastic-plastic J law, respectively.

## Experimental-model cutting plots: effect of cutting speed and constitutive law

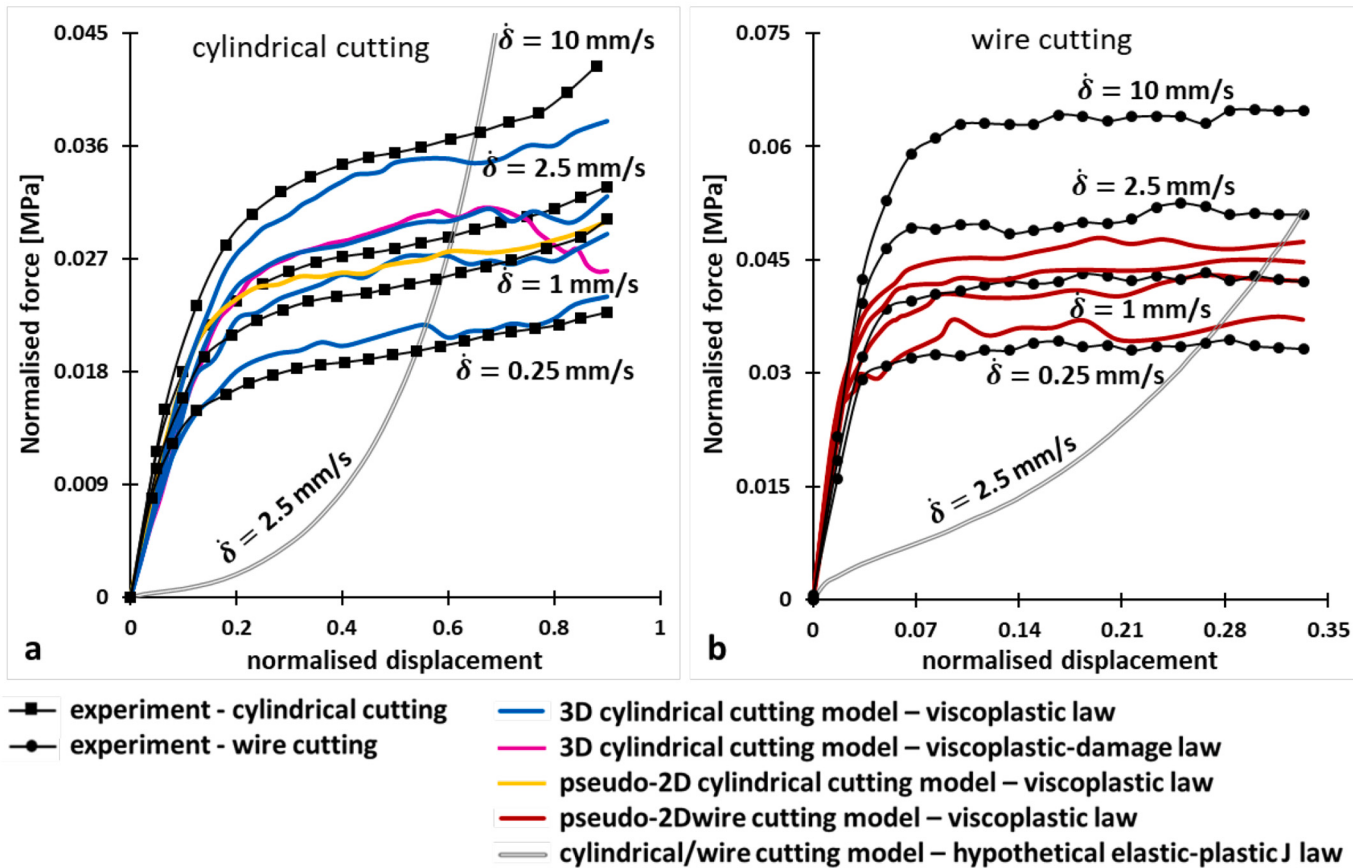


**Fig. 7.** Summary of experimental-FE cutting plots. Plots show: (a) experimental-FE comparison for cylindrical cutting (3D model) in terms of the normalised force,  $F/T_0d_c$  (or  $F/t_0d_w$ ), versus normalised displacement,  $\delta/T_0$  (or  $\delta/t_0$ ), response (for comparability, force is normalised over the product of original specimen thickness and cylinder (or wire) diameter,  $T_0d_c$  (or  $t_0d_w$ ), while displacement is normalised over the original specimen height,  $H_0$  (or  $h_0$ )), (b) corresponding wire cutting experimental-FE results. The FE plots for the four cutting speeds,  $\dot{\delta}$ , correspond to the viscoplastic law, while the prediction based on the hypothetical elastic-plastic J law for  $\dot{\delta} = 2.5 \text{ mm/s}$  is also shown; for  $\dot{\delta} = 2.5 \text{ mm/s}$ , (a) also includes the results based on the viscoplastic-damage law from the 3D model, as well as the results based on the viscoplastic law used within the pseudo-2D cylindrical cutting model.

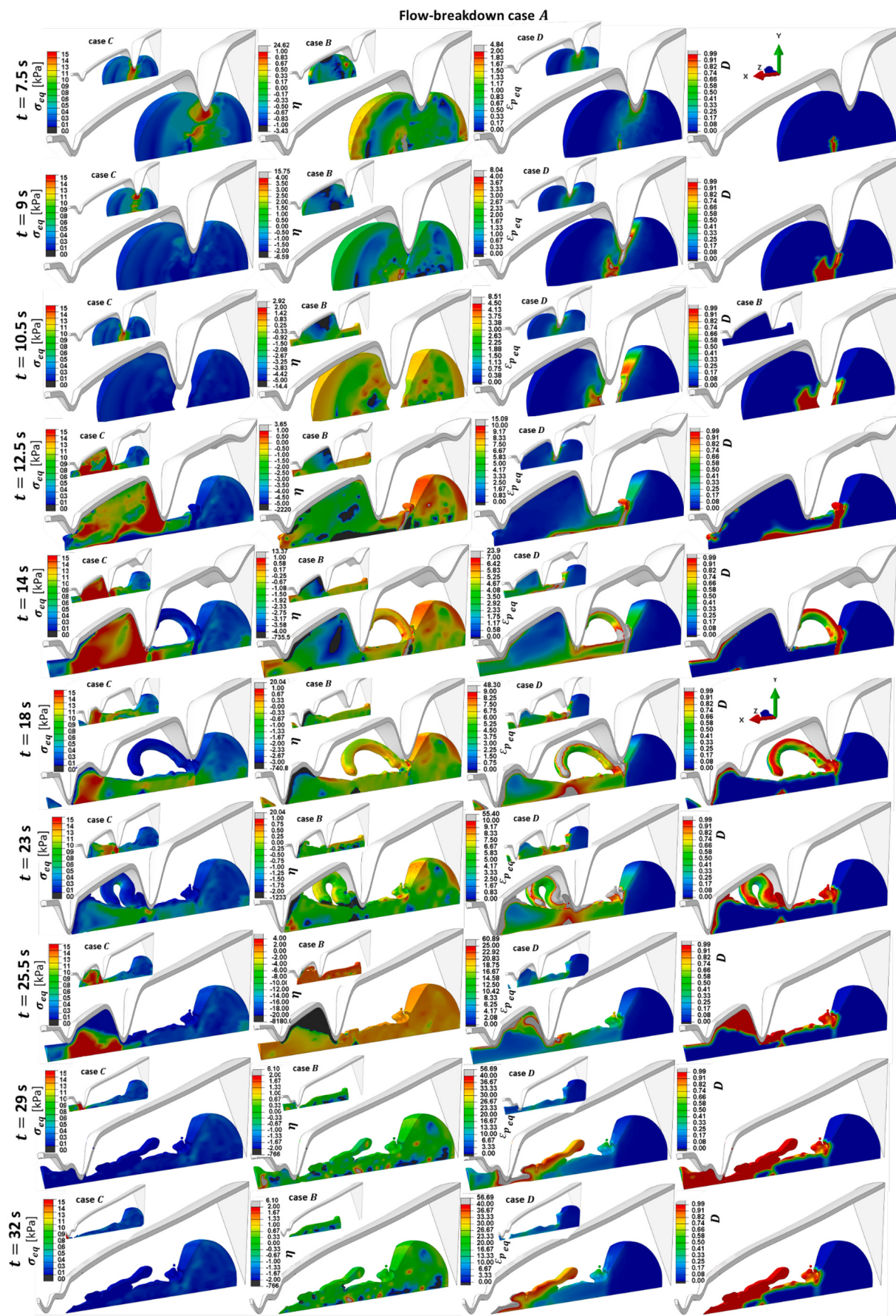
deformation (Figs. 6(a) and 6(e)). Specifically, damage in the form of micro-cracking is found to occur only in the specimen surfaces, surrounding the cylinder/wire, where large stress triaxialities,  $\eta$ , i.e. tensile states, are applied (Skamniotis et al., 2017). However, these micro-cracks are not shown to lead to the creation of macroscopic crack surfaces, and therefore play a minor role in bolus separation; the latter is instead driven by excessive plastic flow of the material surrounding the cutter. These findings suggest that bolus separation here is not described by the classical fracture toughness parameter,  $G_c$  (Skamniotis, Kamaludin, Elliott, Charalambides, 2017).

### 3.2.2. FE cutting results

The 3D cylindrical cutting model is shown to provide accurate predictions in Fig. 7(a) for all speeds and regardless of adding or not adding damage to the viscoplastic law. Specifically, Fig. 7(a) shows that for  $\dot{\delta} = 2.5 \text{ mm/s}$  applying damage (pink curve in Fig. 7(a)) is found to have only a small effect on the predictions which comes into play at large displacements i.e.  $\delta/H_c > 0.7$  (the same is found for the other three speeds - not shown). This is because only occurs at the specimen external surfaces surrounding the cylinder, where tensile states i.e.  $\eta \geq 0.2$ , apply. This is demonstrated by the damage variable,  $D$ , contours in Fig. 6(b), which are also in excellent agreement with the regions where microcracking is observed in the experiment (see Fig. 6(a)). Due to the above, it was sensible not to consider damage in the pseudo-2D cylindrical and pseudo-2D wire cutting models. In fact, the pseudo-2D

cylindrical cutting model is shown (yellow curve in Fig. 7(a)) to provide similar results with the corresponding 3D model. This provides further evidence that cutting here is dominated by excessive plastic flow under plane strain conditions and negative stress triaxialities i.e. highly compressive states.

As opposed to cylindrical cutting, wire cutting (Fig. 7(b)) is not predicted well for the two highest speeds,  $\dot{\delta} = 2.5 \text{ mm/s}$  and  $\dot{\delta} = 10 \text{ mm/s}$  (no damage used in the viscoplastic law). This is because for the above speeds the corresponding strain rates applied locally in the wire cutting region fall outside the experimental rate range,  $0.01/\text{s} - 1/\text{s}$ , based on which the viscoplastic law was calibrated. Specifically, for  $\dot{\delta} = 10 \text{ mm/s}$ , typical rates of the order of  $\dot{\varepsilon}_{eq} = 30/\text{s}$  were found during steady state wire cutting, as opposed to rates of  $\dot{\varepsilon}_{eq} = 2/\text{s}$  in cylindrical cutting, which only slightly exceed the calibration range. This difference between cylindrical and wire cutting is indeed anticipated, since the applied strain rate field is fundamentally expected to scale with the ratio of cutting speed over the cutting diameter,  $\dot{\delta}/d_c$  (or  $\dot{\delta}/d_c$  for wire cutting). This now explains why although the same  $\dot{\delta}$  range is applied in the two tests, wire cutting displays significantly higher experimental normalised forces than cylindrical cutting. On the other hand, it should be noted that high strain rates of  $30/\text{s}$  are expected to occur in the earlier stages of the digestion process, such as during oral processing (Stokes et al. 2013) as well as in the esophageal region i.e. after swallowing (Li et al. 1992). Consequently, the above experimental-model disagreement for wire cutting was not investigated further, since for the rates,  $0.01/\text{s} - 1/\text{s}$



(caption on next page)

**Fig. 8.** Illustration of bolus flow-breakdown FE contours, over ten characteristic times of the gastric process,  $t = 7.5$  s, 9 s, 10.5 s, 12.5 s, 14 s, 18 s, 23 s, 25.5 s, 29 s, 32 s. From left to right, and for bolus flow-breakdown case A, the contours show: equivalent stress,  $\sigma_{eq}$ , stress triaxiality,  $\eta$ , equivalent plastic strain,  $\epsilon_{peq}$ , and damage variable, D. Smaller inset images also show  $\sigma_{eq}$ ,  $\eta$  and  $\epsilon_{peq}$  contours for cases C, B and D, respectively.

s, and speeds,  $\dot{\delta} \leq 2.5$  mm/s, which are more relevant to gastric processing (Shelat et al., 2015; Wu et al., 2016), the model leads to accurate predictions (Fig. 7(b)). Furthermore, our study demonstrates that the bolus deformation-separation processes occurring between the small (wire diameter,  $d_w = 0.5$  mm) and large (cylinder diameter,  $d_c = 5$  mm) cutting length scales can be accurately simulated based on the same viscoplastic law; this simultaneously validates the assumption of continuity in the bolus material.

On the other hand, Figs. 6(d) and Figs. 6(g) illustrate that the above cutting predictions change remarkably when the hypothetical elastic-plastic J law is implemented. Specifically, Figs. 6(d) and 6(g) depict deformations occurring over a large fraction of the specimen's volume when the hypothetical elastic-plastic J law is used, in contrast to the localised flow shown in the corresponding results in Figs. 6(c) and 6(f) based on the viscoplastic law. These differences are reflected in Figs. 7(a-b) in terms of a cylindrical/wire cutting force which increases exponentially with displacement based on the hypothetical elastic-plastic J law. As a result, a hypothetical bolus with the 'J' shaped  $\sigma_{eq} - \epsilon_{eq}$  response exhibits remarkably higher resistance against cutting-flow when compared to the oatcake bolus investigated here.

### 3.3. Gastric flow-breakdown results

#### 3.3.1. Outline

Fig. 8 illustrates the gastric model predictions in terms of equivalent stress,  $\sigma_{eq}$ , equivalent stress triaxiality,  $\eta$ , plastic strain,  $\epsilon_{peq}$ , and damage variable, D, contours over ten characteristic time stages of the simulation. The large images correspond to case A (viscoplastic-damage law and stomach-bolus friction coefficient,  $\mu = 0.9$ ) whereas the small inset images are used to illustrate the corresponding  $\eta$  fields for case B (viscoplastic-damage law and frictionless stomach-bolus contact),  $\sigma_{eq}$  fields for case C (viscoplastic law and  $\mu = 0.9$ ), as well as  $\epsilon_{peq}$  fields for case D (hypothetical elastic-plastic J law and  $\mu = 0.9$ ), to enable comparisons between the four gastric bolus flow-breakdown cases. The evolution of total force generated due to bolus-stomach wall contact is plotted for all cases A – D in Fig. 9(a); the latter encapsulates force due to contact pressure as well as frictional shear stress. On the other hand, Figs. 9(b) and 9(c) respectively show the evolution of external work and percentage bolus mass retained in the stomach. The total force and external work results are output directly from ABAQUS (Simulia, 2013); however, in Figs. 8(a) and 8(b) we present these results normalised over the bolus original mass,  $m_b = 9.8$  g, and scaled by a factor of 12 i.e. data translated from the reduced model (30° segment) into the actual gastric geometry. In addition, external work associated with deformation of the stomach wall (necessary for applying ACWs) is subtracted i.e. it is not encapsulated in the plots of 8(b), since the above here depends on the arbitrarily chosen VDW hyperelastic law parameters (Section 2.3.2).

#### 3.3.2. Flow-breakdown patterns for case A

For case A, Fig. 8 ( $t = 7.5$  s) shows that the occlusion of the first ACW generates highly tensile states ( $\eta > 1$ ) in the core of the bolus, such that in the respective region damage starts to evolve. Thereafter at  $t = 9$  s, fracture initiates leading to complete bolus separation into two fragments at  $t = 10.5$  s; at this instance full unloading occurs i.e.  $\sigma_{eq} \approx 0$  in the entire bolus (and corresponding reduction in forces in Fig. 9(a)). Due to the absence of gravity, any small amount of kinetic energy induced by fracture causes the bolus fragment which loses contact with the ACW (on the right) to move backwards. Its motion is however constrained here by the rigid bounding shell such that the material eventually resides at a constant position for the rest of the gastric process; in reality, the motion of the respective fragment would be

instead dictated by the surrounding liquid flow-pressure and/or gravity (Cleary et al., 2015). On the other hand, the fragment which remains in contact with the ACW (on the left) is transported towards the pylorus and at  $t = 12.5$  s it is squeezed between the first ACW and the open sphincter. The latter causes a dramatic increase in contact forces (Fig. 9(a)), such that the external work also elevates (see Fig. 9(b)). The squeezed material undergoes highly compressive stress states i.e.  $\eta < -3$ , including areas of extreme confinement i.e.  $\eta = -2220$ , accompanied by excessive strains i.e.  $\epsilon_{peq} = 15$ . These results highlight that the bulk modulus, K, as well as the  $\sigma_{eq} - \epsilon_{eq}$  response at extreme compressive strains may play a significant role in bolus flow at the pyloric region.

Simultaneously bolus squeezing at  $t = 12.5$  s leads to the onset of material outflow through the sphincter (see onset of mass reduction in Fig. 9(c)), as well as significant backward extrusion (jet-like retro-pulsive motion), both occurring at an approximately common speed of 20 mm/s (in the  $-X$  direction); the latter is in reasonable agreement with the value 28 mm/s predicted by Ferrua et al. (Ferrua & Singh, 2010), adding credibility to the study. As a result of backward extrusion, Eulerian-Eulerian contact occurs between the extruded material (left) and the stationary bolus fragment (right). The contact interface between the two bodies manifests itself in the form of a damage band, which is encountered due to very large tensile strains i.e.  $\epsilon_{peq} = 15$  and  $\eta = 3.65$  ( $t = 12.5$  s). As backward extrusion continues ( $t = 14$  s) the material escapes from the above contact interface in the form of a curled strip, which is then detached from the remaining body of the bolus, at  $t = 18$  s, through contact with the second ACW. It is worth mentioning that while the second ACW approaches very close to the stationary bolus fragment, contact does not occur and therefore a second fracture event, similar to the one at  $t = 9 - 10.5$  s, does not take place. This may not be relevant to in-vivo functions, in the sense that ACW can in fact initiate from various locations in the stomach such that breakdown occurs in a more efficient manner.

At  $t = 18$  s, the sphincter closes and the first ACW also starts retracting into zero occlusion. Instantly, this causes unloading (overall reduction in  $\sigma_{eq}$  and contact force), while backward extrusion stops such that the Eulerian-Eulerian contact interface between the initial two bolus fragments (seen earlier at  $t = 12.5 - 14$  s) vanishes. Instead, the corresponding material sticks together, such that tensile stress can be transmitted across the interface i.e. bolus re-agglomeration. This is an inevitable numerical phenomenon of Eulerian-Eulerian contact, which owes to the kinematic assumption of a unique deformation state for all the materials included within a Eulerian element. Based on the features modelled here, at  $t = 23$  s the curled strip along with the neighbouring material are squeezed together between the second ACW and the closed sphincter, and thus form a continuum bolus mass at  $t = 25.5$  s. Upon sphincter re-opening ( $t = 25.5$  s), the latter eventually flows outside the Eulerian domain, as illustrated at  $t = 29$  s in Fig. 8, such that at  $t = 32$  s the mass retained in the stomach is reduced further i.e. compare retained mass between  $t = 29$  s and  $t = 32$  s in Fig. 9(c).

#### 3.3.3. Comparing flow-breakdown cases

The bolus flow-breakdown patterns described above for case A are found to change considerably when the flow-breakdown cases B, C and D are modelled. An important finding is that the frictionless stomach-bolus contact in case B does not allow for sufficiently large tensile strains to be applied in the bolus, such that damage initiation and subsequent fracture never occur; the same is observed in cases C – D for which no damage is used in the constitutive law. The frictionless condition in case B also leads to bolus-gastric wall slip at  $t < 7.5$  s, such that the occlusion of the first ACW does not indent in the bulk of the bolus, but instead the bolus is directly transported towards the

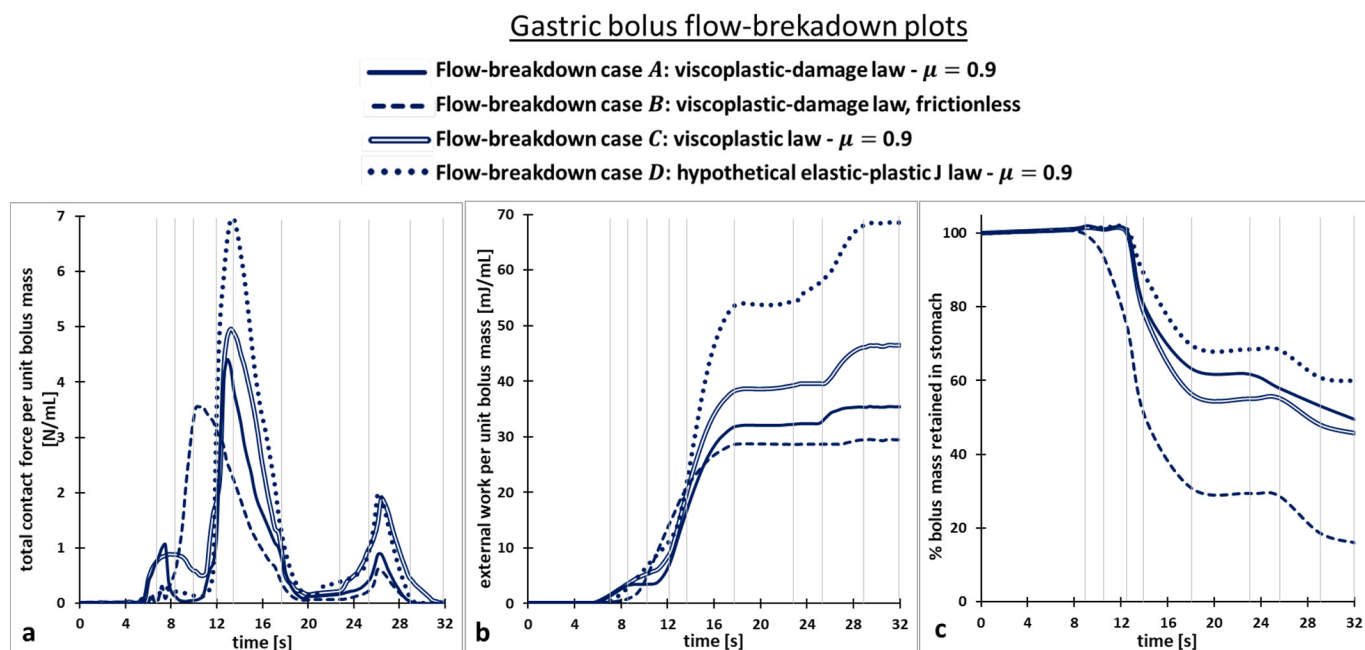


**Fig. 9.** Summary of predicted output variables of the gastric model. Plots show: (a) comparison of total bolus-gastric wall contact force per unit bolus mass versus time between flow-breakdown cases A – D, (b) comparison of external work per unit bolus mass versus time between bolus flow-breakdown cases A – D, (c) comparison of percentage bolus mass retained in stomach versus time between cases A – D (mass preservation is satisfied within 2% maximum numerical error at time  $t = 12.5$  s, i.e. 3% mass increase).

sphincter (see scenario B at  $t = 9$  s). This explains the lowest values of contact force (Fig. 9(a)) and external work (Fig. 9(b)) for case B, amongst all the other scenarios, and simultaneously the highest, by far, degree of stomach emptying (Fig. 9(c)). It therefore appears that the efficiency of bolus transport from the stomach into the small intestine decreases with friction. Nevertheless, this can be a misleading result, as in reality, prior to gastric emptying bolus breakdown is required (Kong & Singh, 2008), for which friction is shown to be necessary here i.e. no damage occurs for frictionless condition. On the other hand, Figs. 9(a) and 9(b) demonstrate that a ‘J’ shaped stress-strain bolus behaviour (case D) clearly enhances contact forces and external work remarkably, compared to the perfectly plastic (rate dependent) constitutive behaviour of the oatcake bolus. These results are consistent with the wire-cylindrical cutting experiments (Figs. 7(a-b) – Section 3.2.3) where the cutting forces increased sharply with cutting displacement, due to the high resistance of the hypothetical bolus (with ‘J’ shaped response) against deformation. Regarding differences in the gastric flow-breakdown results between using damage or not i.e. case A versus case C, these are less clear in Figs. 9a-c. Specifically, case C displays higher external work due to the absence of fracture (no damage used) (see Fig. 9(b)), but the bolus mass retained in the stomach is only slightly lower than case A (see Fig. 9(c)). The latter is attributed to the combination of the following facts: (a) again that gastric emptying occurs through prescribed gastric motility patterns (including pyloric sphincter and ACWs), and, (b) that when fracture occurs (case A), the corresponding bolus fragments re-agglomerate (discussed earlier) such that the effect of fracture on the overall bolus behaviour is small.

#### 4. General discussion-evaluation

In this final section we evaluate and discuss the important attributes our gastric modelling approach, including its merits, its main limitations as well as features than can be readily incorporated in extended versions of the gastric FE model.

One limitation of the current gastric model is that the requirement for bolus breakdown prior to gastric emptying is not taken into account, since both the ACWs as well as the pyloric sphincter opening-closing are

applied in terms of prescribed displacement histories. As a result, the pyloric sphincter opens and closes independently, regardless of what is happening in the stomach, such that our model likely leads to overestimated gastric emptying rates. Consequently, at this stage Fig. 9(a-c) can only indicate the individual effects of stomach-bolus friction and bolus constitutive law on the total contact force (Fig. 9(a)), external work (Fig. 9(b)) and, more importantly, bolus transport-deformation-fracture behaviour within the stomach (Fig. 9(c)). This shortcoming highlights the need for: (a) incorporating in the model a mechanism that takes into account the bolus size reduction i.e. increase of bolus free surface to volume ratio, before material is allowed to outflow through the pylorus. Incorporating feedback mechanisms will be considered in future study.

Another limitation of the gastric model is that upon bolus separation-fracture, the corresponding bolus fragments re-agglomerate such that the effect of fracture on the overall bolus behaviour is underpredicted. The actual extent and significance of bolus re-agglomeration during in-vivo gastric digestion remains unknown. From a numerical modelling perspective, the sticking between bolus fragments shown here, can be avoided through deploying a more elaborative model where the void regions between bolus and stomach are filled with a liquid phase. In this case, the numerical sticking phenomenon would likely occur between the free surfaces of the bolus and the surrounding liquid phase, which appears to be a more realistic condition. This simultaneously creates the opportunity for modelling hydration and/or chemical degradation effects i.e. bolus material softening due to interaction with liquids/acids/enzymes (Bornhorst et al., 2016; Cleary et al., 2015). Including a liquid environment in the gastric model will also allow exploring the extend at which ACWs can induce critical pressures between the liquid and the bolus that can also potentially induce breakdown.

At this point, it should be underlined that breakdown-fracture is here investigated based on the damage parameters calibrated specifically for the moisture content,  $M_{\%} = 50\%$ . The latter was chosen because it led to an interesting material state, which included features from both liquids i.e. low shear resistance and solids i.e. macroscopic fracture under tensile states. The presence of both of these features

allowed us to test the capability of the Eulerian FE approach in modelling and providing a comprehensive description of the various deformation-fracture macroscopic phenomena that can arise upon food bolus deformation. However, as moisture content increases in the gastric environment i.e. beyond 60%, classical macroscopic fracture phenomena that typically occur in solids are not expected (discussed in Section 2.1). Consequently, modelling crack propagation for the particular oatcake system may be only relevant to the initial stages of gastric breakdown.

Regardless of whether bolus separation occurs in a solid-like i.e. crack propagation, or liquid-like manner, our model generally indicates that a liquid (and acidic) environment will aid in obtaining realistic numbers on the evolution of total bolus free surface over volume ratio, towards evaluating true gastric emptying rates. A profound implication of the absence of liquid environment in the model here is that although in case A the retained mass in Fig. 9(c) is eventually 50% ( $t = 32$  s) of the initial value at  $t = 7.5$  s, this does not imply that the total external/free surface area of the remaining bolus is decreased in a proportional manner. This is because as evidenced by Fig. 8 at  $t = 32$  s for all flow-breakdown cases A – D, the retained mass deforms excessively which generally tends to increase the total external bolus surface area. For instance, in case A, the total external bolus surface area is calculated to decrease by a total of only 18% (approximately) at the end of the simulation; this should be compared to the theoretical reduction of 37% in the total surface area associated with a volumetric and/or mass (the same for constant density) decrease of 50% in a sphere which retains its spherical shape. A similar trend is found for the rest of scenarios, B, C and D, in terms of the ratio between the percentage decrease of retained bolus mass and the corresponding decrease in external bolus surface area. The calculation of this ratio imposes the question of how bolus re-agglomeration should be regarded, which indicates the need for including a liquid environment in the gastric flow-breakdown simulations.

Amongst the encouraging results of the study here, one is the fact that the differences in the bolus-gastric wall contact forces and total external work output in Figs. 9(a) and 9(b), between the viscoplastic law (oatcake bolus) and the 'J' shaped law (hypothetical bolus), correlate closely with the differences in the corresponding wire-cylindrical cutting forces in Figs. 7(a-b) – Section 3.2.3, as well as the rheological stress-strain responses (uniaxial compression) in Fig. 4(c). This suggests that the wire-cylindrical cutting tests can provide useful indications in terms of the potential flow-breakdown response of the bolus at initial stages of digestion, in a rather straightforward manner. One reason for studying the hypothetical 'J' shaped response here is to reinforce the message that a strong relevance exists between the uniaxial stress-strain bolus response, the wire-cylindrical cutting response and the gastric flow-breakdown response predictions. Another reason is to provide comparisons against the true viscoplastic-damage flow-breakdown response of the oatcake bolus, showcasing the potential implications of a bolus with high resistance against deformation i.e. 'J' shaped hyperelastic/rubber-like behaviour. Such in-vivo bolus states, characterised by a highly cohesive and/or hard texture i.e. high shear modulus and/or gel strength, can be expected for less hydrophilic solid foods with pronounced internal structural integrity, such as non-cooked vegetables, cheese and meat (Ishihara, Nakauma, Funami, Odake, & Nishinari, 2011). In this regard, our results on the extreme scenario of a hypothetical hyperelastic 'J' shaped response here, simultaneously demonstrate the capability of the Eulerian FE approach in simulating such scenarios; note that this approach can also be of use in studies related to dysphagia (Assad-Bustillos, Tournier, Septier, Della Valle, & Feron, 2019; Lorieau et al., 2018). It should be mentioned, however, that the above examples of less hydrophilic foods simultaneously imply potentially increased discontinuity-heterogeneity in the bolus, particularly after swallowing. This generates the question as to whether our entire experimental-modelling approach used here, based on a continuous-homogeneous, water saturated oatcake bolus, remains suitable for such

cases. From a computational modelling perspective, the answer is that the Eulerian FE approach is shown able to capture both a semi-solid/fluidic response i.e. low shear resistance (viscoplastic law for oatcake bolus) and a solid response i.e. high shear resistance ('J' shaped law for hypothetical bolus). In this case, our constitutive modelling techniques remain applicable, in the sense that the type of viscoplastic law calibrated here for the oatcake bolus, can also be calibrated to model water or saliva within the bolus suspension (i.e. by using a low shear/young's modulus and low yield stresses); in the same manner, the viscoplastic and/or 'J' law can be calibrated to describe the hydrophobic solid fragments in the bolus suspension. These individual constitutive responses can be simulated together within our gastric model, by defining explicitly an initial double-phase bolus in the Eulerian FE domain, in which the solid and semi-solid/fluidic phases move/deform and interact with each other under applied ACWs. To take advantage of this numerical capability, one may not obtain a continuous bolus by mixing the solid and fluidic phases, but instead measure the rheology of each phase separately. Conclusively, although in this study we have used an artificial continuum bolus for the rather hydrophilic oatcake system, the solid mechanics principles and the Eulerian FE modelling approach remain applicable in heterogeneous boluses with discrete solid and liquid phases.

## 5. Conclusions

Our study aims to advance the available knowledge and technology in characterising and modelling food deformation-fracture in the stomach. We believe that these advances are important in the development of new tools to aid the design of new functional foods with controlled digestive performance towards improving human health.

Food bolus specimens formed via mixing biscuit particles with water, such that the liquid to solid ratios lied in the range 40–60%, are used to mimic food after the oral process. Although this idealisation may not capture the complexity of a real human bolus, yet it provides a starting point for introducing continuum solid mechanics concepts into the process of digestion. Uniaxial compression tests reveal a typical viscoplastic stress-strain bolus behaviour which is verified through shear (rotational) rheometry; the latter is found weak in extracting material data at large strains, particularly at low liquid to solid ratios. We utilise the experimental data to calibrate a viscoplastic law which we verify by simulating accurately additional bolus cutting experiments performed at various rates and at two cutting length scales i.e. large cylindrical and small wire cutting tools, through the Eulerian FE analysis. This validates our continuum solid mechanics approach and also indicates that a material damage/fracture criterion is not required for modelling bolus separation when this is dominated by large local plastic deformation and tensile strains remain small.

In contrast, our gastric processing model reveals that a damage criterion is necessary in predicting fracture in the bolus as the latter is deformed by contraction waves. This owes to much higher applied tensile states compared to cylindrical/wire cutting, particularly when friction between the gastric wall and bolus is severe. Our model however predicts that bolus fragments stick again together after fracture, such that eventually the total bolus free surface to volume ratio only changes slightly. This suggests that in reality, together with contraction waves, gastric liquids may also play a role in preventing bolus agglomeration such that bolus size reduction and associated chemical-hydration processes are less obstructed.

Our study provides key information on the mechanical breakdown of solid meals during gastric processing. These advances will frame the development of integrated *in-silico* as well as *in-vitro* models that can inform food design for engineered digestive performance.

## Industrial relevance

Nowadays, there is strong industrial interest in manipulating not

only the behaviour of food in the mouth towards enhancing consumer preference, but also the response of food in the GI tract, in order to address satiety, obesity and generally health related concerns. Our computational tools and entire gastric modelling strategy here, can be applied in a wide range of food systems, in order to predict, cost-effectively, bolus cohesive behaviour and associated bolus size reduction rates in the stomach. The advantage of this *in-silico* approach is that the predictions rely on standardised food bolus mechanical properties i.e. stress-strain curve, that can be measured independently. These bolus properties, post swallowing, can be related to original food properties prior to ingestion i.e. micro-structure, macro-geometry, ingredients, providing a scientific rational for designing food products that satisfy both palatability and digestibility-nutritional criteria.

### Declaration of Competing Interest

The authors declare that they have no known competing financial interests or personal relationships that could have appeared to influence the work reported in this paper.

### Acknowledgements

BBSRC is acknowledged for funding this research (grant number: BB/P023851/1). The academic partner Prof Alan Mackie, and industrial collaborators associated with Nestle, Mondelez International and PepsiCo are acknowledged for providing useful feedback throughout the study. Dr Guy Della Valle is acknowledged for obtaining rheological data on food systems relevant to the study and providing useful interpretations of these results. Ruth Brooker is also acknowledged for providing training on the experimental apparatus.

### Appendix A. Supplementary data

Supplementary data to this article can be found online at <https://doi.org/10.1016/j.ifset.2020.102510>.

### References

- Abrahamsson, B., Albery, T., Eriksson, A., Gustafsson, I., & Sjöberg, M. (2004). Food effects on tablet disintegration. *European Journal of Pharmaceutical Sciences*, 22(2–3), 165–172.
- Alokaily, S., Feigl, K., & Tanner, F. X. (2019). Characterization of peristaltic flow during the mixing process in a model human stomach. *Physics of Fluids*, 31(10), 103105.
- Assad-Bustillos, M., Tournier, C., Septier, C., Della Valle, G., & Feron, G. (2019). Relationships of oral comfort perception and bolus properties in the elderly with salivary flow rate and oral health status for two soft cereal foods. *Food Research International*, 118, 13–21.
- Augustin, L. S., Franceschi, S., Jenkins, D. J., Kendall, C. W., & La Vecchia, C. (2002). Glycemic index in chronic disease: A review. *European Journal of Clinical Nutrition*, 56(11), 1049–1071.
- Avantaggiato, G., Havenaar, R., & Visconti, A. (2003). Assessing the zearalenone-binding activity of adsorbent materials during passage through a dynamic *in vitro* gastrointestinal model. *Food and Chemical Toxicology*, 41(10), 1283–1290.
- Bahado-Singh, P. S., Riley, C. K., Wheatley, A. O., & Lowe, H. I. (2011). Relationship between processing method and the glycemic indices of ten sweet potato (*Ipomoea batatas*) cultivars commonly consumed in Jamaica. *Journal of Nutrition and Metabolism*, 2011.
- Benson, D. J. (2000). An implicit multi-material Eulerian formulation. *International Journal for Numerical Methods in Engineering*, 48(4), 475–499.
- Benson, D. J., & Okazawa, S. (2004). Contact in a multi-material Eulerian finite element formulation. *Computer Methods in Applied Mechanics and Engineering*, 193(39–41), 4277–4298.
- Berry, R., Miyagawa, T., Paskaranandavadiel, N., Du, P., Angeli, T. R., Trew, M. L., ... Cheng, L. K. (2016). Functional physiology of the human terminal antrum defined by high-resolution electrical mapping and computational modeling. *American Journal of Physiology. Gastrointestinal and Liver Physiology*, 311(5), G895–G902.
- Björck, I., Granfeldt, Y., Liljeberg, H., Tovar, J., & Asp, N. G. (1994). Food properties affecting the digestion and absorption of carbohydrates. *The American Journal of Clinical Nutrition*, 59(3), 699S–705S.
- Björklund, M., Ouwehand, A. C., & Forsten, S. D. (2011). Improved artificial saliva for studying the cariogenic effect of carbohydrates. *Current Microbiology*, 63(1), 46–49.
- Bohn, T., Carriere, F., Day, L., Deglaire, A., Egger, L., Freitas, D., ... Menard, O. (2018). Correlation between *in vitro* and *in vivo* data on food digestion. What can we predict with static *in vitro* digestion models? *Critical Reviews in Food Science and Nutrition*, 58(13), 2239–2261.
- Bornhorst, G. M., & Singh, R. P. (2013). Kinetics of *in vitro* bread bolus digestion with varying oral and gastric digestion parameters. *Food Biophysics*, 8(1), 50–59.
- Bornhorst, G. M., Gousseti, O., Wickham, M. S., & Bakalis, S. (2016). Engineering digestion: Multiscale processes of food digestion. *Journal of Food Science*, 81(3), R534–R543.
- Brand, J. C., Nicholson, P. L., Thorburn, A. W., & Truswell, A. S. (1985). Food processing and the glycemic index. *The American Journal of Clinical Nutrition*, 42(6), 1192–1196.
- Brodkorb, A., Egger, L., Alminger, M., Alvito, P., Assuncao, R., Ballance, S., ... Recio, I. (2019). INFOGEST static *in vitro* simulation of gastrointestinal food digestion. *Nature Protocols*, 14(4), 991–1014.
- Brouns, F., Björck, I., Frayn, K., Gibbs, A., Lang, V., Slama, G., & Wolever, T. (2005). Glycaemic index methodology. *Nutrition Research Reviews*, 18(1), 145–171.
- Charalambides, M., Goh, S., Wanigasooriya, L., Williams, J., & Xiao, W. (2005). Effect of friction on uniaxial compression of bread dough. *Journal of Materials Science*, 40(13), 3375–3381.
- Chen, J. (2009). Food oral processing—A review. *Food Hydrocolloids*, 23(1), 1–25.
- Cleary, P., Sinnott, M., Hari, B., Bakalis, S., & Harrison, S. (2015). *Modelling food digestion. Modeling food processing operations*. Woodhead Publishing Series in Food Science, Technology and Nutrition. Woodhead Publishing 255–305.
- De Cock, N., Massinon, M., Mercatoris, B., & Lebeau, F. (2014). *Numerical modelling of mirror nozzle flow. 2014 Montreal, Quebec Canada July 13–July 16, 2014*. American Society of Agricultural and Biological Engineers.
- Documentation, S. (2010). *SolidWorks simulation premium: Nonlinear*. (Training Manual Serial No).
- Drechsler, K. C., & Bornhorst, G. M. (2018). Modeling the softening of carbohydrate-based foods during simulated gastric digestion. *Journal of Food Engineering*, 222, 38–48.
- Drechsler, K. C., & Ferrua, M. J. (2016). Modelling the breakdown mechanics of solid foods during gastric digestion. *Food Research International*, 88, 181–190.
- Drucker, D. C. (1957). *A definition of stable inelastic material*. BROWN UNIV PROVIDENCE RI.
- Dupont, D., Alric, M., Blanquet-Diot, S., Bornhorst, G., Cueva, C., Deglaire, A., ... Lelieveld, J. (2019). Can dynamic *in vitro* digestion systems mimic the physiological reality? *Critical Reviews in Food Science and Nutrition*, 59(10), 1546–1562.
- Feinle, C., Kunz, P., Boesiger, P., Fried, M., & Schwizer, W. (1999). Scintigraphic validation of a magnetic resonance imaging method to study gastric emptying of a solid meal in humans. *Gut*, 44(1), 106–111.
- Ferrua, M., & Singh, R. (2010). Modeling the fluid dynamics in a human stomach to gain insight of food digestion. *Journal of Food Science*, 75(7), R151–R162.
- Ferrua, M. J., Kong, F., & Singh, R. P. (2011). Computational modeling of gastric digestion and the role of food material properties. *Trends in Food Science & Technology*, 22(9), 480–491.
- Ferrua, M. J., Xue, Z., & Singh, R. P. (2014). On the kinematics and efficiency of advective mixing during gastric digestion—a numerical analysis. *Journal of Biomechanics*, 47(15), 3664–3673.
- Fontanella, C. G., Salmaso, C., Toniolo, I., de Cesare, N., Rubini, A., De Benedictis, G. M., & Carniel, E. L. (2019). Computational models for the mechanical investigation of stomach tissues and structure. *Annals of Biomedical Engineering*, 47(5), 1237–1249.
- Gamopilas, C., Charalambides, M., & Williams, J. (2009). Determination of large deformation and fracture behaviour of starch gels from conventional and wire cutting experiments. *Journal of Materials Science*, 44(18), 4976–4986.
- Guerra, A., Etienne-Mesmin, L., Livrelli, V., Denis, S., Blanquet-Diot, S., & Alric, M. (2012). Relevance and challenges in modeling human gastric and small intestinal digestion. *Trends in Biotechnology*, 30(11), 591–600.
- Harrison, S. M., & Cleary, P. W. (2014). Towards modelling of fluid flow and food breakup by the teeth in the oral cavity using smoothed particle hydrodynamics (SPH). *European Food Research and Technology*, 238(2), 185–215.
- Harrison, S. M., Cleary, P. W., Eyres, G., Sinnott, M. D., & Lundin, L. (2014a). Challenges in computational modelling of food breakdown and flavour release. *Food & Function*, 5(11), 2792–2805.
- Harrison, S. M., Eyres, G., Cleary, P. W., Sinnott, M. D., Delahunt, C., & Lundin, L. (2014b). Computational modeling of food oral breakdown using smoothed particle hydrodynamics. *Journal of Texture Studies*, 45(2), 97–109.
- Hur, S. J., Lim, B. O., Decker, E. A., & McClements, D. J. (2011). In vitro human digestion models for food applications. *Food Chemistry*, 125(1), 1–12.
- Imai, Y., Kobayashi, I., Ishida, S., Ishikawa, T., Buist, M., & Yamaguchi, T. (2013). Antral recirculation in the stomach during gastric mixing. *American Journal of Physiology. Gastrointestinal and Liver Physiology*, 304(5), G536–G542.
- Iqbal, M., Li-Mayer, J., Lewis, D., Connors, S., & Charalambides, M. (2020). Mechanical characterization of the nitrocellulose-based visco-hyperelastic binder in polymer bonded explosives. *Physics of Fluids*, 32(2), Article 023103.
- Ishihara, S., Nakamura, M., Funami, T., Odake, S., & Nishinari, K. (2011). Viscoelastic and fragmentation characters of model bolus from polysaccharide gels after instrumental mastication. *Food Hydrocolloids*, 25(5), 1210–1218.
- Johansson, D. P., Gutiérrez, J. L. V., Landberg, R., Alminger, M., & Langton, M. (2018). Impact of food processing on rye product properties and their *in vitro* digestion. *European Journal of Nutrition*, 57(4), 1651–1666.
- Karthikeyan, J. S., Salvi, D., Corradini, M. G., Ludescher, R. D., & Karwe, M. V. (2019). Effect of bolus viscosity on carbohydrate digestion and glucose absorption processes: An *in vitro* study. *Physics of Fluids*, 31(11), 111905.
- Koistinen, V. M., Mattila, O., Katina, K., Poutanen, K., Aura, A.-M., & Hanhineva, K. (2018). Metabolic profiling of sourdough fermented wheat and rye bread. *Scientific Reports*, 8(1), 1–11.
- Kong, F., & Singh, R. (2008). Disintegration of solid foods in human stomach. *Journal of Food Science*, 73(5).
- Kong, F., & Singh, R. P. (2010). A human gastric simulator (HGS) to study food digestion

- in human stomach. *Journal of Food Science*, 75(9), E627–E635.
- Kozolek, M., Grimm, M., Garbacz, G., Kühn, J.-P., & Weitsches, W. (2014). Intragastric volume changes after intake of a high-caloric, high-fat standard breakfast in healthy human subjects investigated by MRI. *Molecular Pharmaceutics*, 11(5), 1632–1639.
- Kozu, H., Kobayashi, I., Nakajima, M., Uemura, K., Sato, S., & Ichikawa, S. (2010). Analysis of flow phenomena in gastric contents induced by human gastric peristalsis using CFD. *Food Biophysics*, 5(4), 330–336.
- Kwiatek, M. A., Steingoetter, A., Pal, A., Menne, D., Brasseur, J. G., Hebbard, G. S., ... Schwizer, W. (2006). Quantification of distal antral contractile motility in healthy human stomach with magnetic resonance imaging. *Journal of Magnetic Resonance Imaging*, 24(5), 1101–1109.
- Le Bleis, F., Chaunier, L., Montigaud, P., & Della Valle, G. (2016). Destructuration mechanisms of bread enriched with fibers during mastication. *Food Research International*, 80, 1–11.
- Le Feunteun, S., Barbé, F., Rémond, D., Ménard, O., Le Gouar, Y., Dupont, D., & Laroche, B. (2014). Impact of the dairy matrix structure on milk protein digestion kinetics: Mechanistic modelling based on mini-pig *in vivo* data. *Food and Bioprocess Technology*, 7(4), 1099–1113.
- Le Feunteun, S., Mackie, A. R., & Dupont, D. (2020). In silico trials of food digestion and absorption: How far are we? *Current Opinion in Food Science*, 121–125.
- Li, M., Brasseur, J. G., Kern, M. K., & Dodds, W. J. (1992). Viscosity measurements of barium sulfate mixtures for use in motility studies of the pharynx and esophagus. *Dysphagia*, 7(1), 17–30.
- Lorieau, L., Septier, C., Laguerre, A., Le Roux, L., Hazart, E., Ligneul, A., Famelart, M.-H., Dupont, D., Floury, J., & Feron, G. (2018). Bolus quality and food comfortability of model cheeses for the elderly as influenced by their texture. *Food Research International*, 111, 31–38.
- Lundin, L., Golding, M., & Wooster, T. J. (2008). Understanding food structure and function in developing food for appetite control. *Nutrition and Dietetics*, 65, S79–S85.
- Mackie, A. R., Rafiee, H., Malcolm, P., Salt, L., & van Aken, G. (2013). Specific food structures suppress appetite through reduced gastric emptying rate. *American Journal of Physiology. Gastrointestinal and Liver Physiology*, 304(11), G1038–G1043.
- Marciani, L., Pritchard, S. E., Hellier-Woods, C., Costigan, C., Hoad, C., Gowland, P. A., & Spiller, R. C. (2013). Delayed gastric emptying and reduced postprandial small bowel water content of equocaloric whole meal bread versus rice meals in healthy subjects: Novel MRI insights. *European Journal of Clinical Nutrition*, 67(7), 754–758.
- McClements, D. J., & Li, Y. (2010). Review of *in vitro* digestion models for rapid screening of emulsion-based systems. *Food & Function*, 1(1), 32–59.
- Ménard, O., Cattenoz, T., Guillemin, H., Souchon, I., Deglaire, A., Dupont, D., & Picque, D. (2014). Validation of a new *in vitro* dynamic system to simulate infant digestion. *Food Chemistry*, 145, 1039–1045.
- Minekus, M., Marteau, P., & Havenaar, R. (1995). Multicompartmental dynamic computer-controlled model simulating the stomach and small intestine. Alternatives to laboratory animals: ATLA.
- Minekus, M., Alminger, M., Alvito, P., Ballance, S., Bohn, T., Bourlieu, C., ... Dupont, D. (2014). A standardised static *in vitro* digestion method suitable for food—an international consensus. *Food & Function*, 5(6), 1113–1124.
- Mohammed, M. A. P., Tarleton, E., Charalambides, M. N., & Williams, J. (2013). Mechanical characterization and micromechanical modeling of bread dough. *Journal of Rheology*, 57(1), 249–272.
- Mohammed, I. K., Skamniotis, C. G., & Charalambides, M. N. (2019 Oct 17). Developing Food Structure for Mechanical Performance. *Handbook of Food Structure Development* 18:199.
- Moxon, T., Gouseti, O., & Bakalis, S. (2016). In silico modelling of mass transfer & absorption in the human gut. *Journal of Food Engineering*, 176, 110–120.
- Ng, T. S., McKinley, G. H., & Padmanabhan, M. (2007). Linear to non-linear rheology of wheat flour dough.
- Overduin, J., Guérin-Deremaux, L., Wils, D., & Lamberts, T. T. (2015). NUTRALYS® pea protein: Characterization of *in vitro* gastric digestion and *in vivo* gastrointestinal peptide responses relevant to satiety. *Food & Nutrition Research*, 59(1), 25622.
- Ozvural, E. B., & Bornhorst, G. M. (2018). Chemical and structural characteristics of frankfurters during *in vitro* gastric digestion as influenced by cooking method and severity. *Journal of Food Engineering*, 229, 102–108.
- Pal, A., Brasseur, J. G., & Abrahamsson, B. (2007). A stomach road or “Magenstrasse” for gastric emptying. *Journal of Biomechanics*, 40(6), 1202–1210.
- Potti, J. M., Braga, B., & Qin, B. (2017). Ultra-processed food intake and obesity: What really matters for health-processing or nutrient content? *Current Obesity Reports*, 6(4), 420–431.
- Prinz, J., & Heath, M. (2000). Bolus dimensions in normal chewing. *Journal of Oral Rehabilitation*, 27(9), 765–768.
- Prinz, J. F., & Lucas, P. W. (1997). An optimization model for mastication and swallowing in mammals. *Proceedings of the Royal Society of London. Series B: Biological Sciences*, 264(1389), 1715–1721.
- Puls, H., Klocke, F., & Lung, D. (2014). Experimental investigation on friction under metal cutting conditions. *Wear*, 310(1–2), 63–71.
- Razdan, A., & Pettersson, D. (1996). Hypolipidaemic, gastrointestinal and related responses of broiler chickens to chitosans of different viscosity. *British Journal of Nutrition*, 76(3), 387–397.
- Rush, J. W., Jantzi, P. S., Dupak, K., Idziak, S. H., & Marangoni, A. G. (2008). Effect of food preparation on the structure and metabolic responses to a monostearin-oil–water gel-based spread. *Food Research International*, 41(10), 1065–1071.
- Schwingenschäckl, L., & Hoffmann, G. (2013). Long-term effects of low glycemic index/load vs. high glycemic index/load diets on parameters of obesity and obesity-associated risks: A systematic review and meta-analysis. *Nutrition, Metabolism, and Cardiovascular Diseases*, 23(8), 699–706.
- Shelat, K. J., Nicholson, T., Flanagan, B. M., Zhang, D., Williams, B. A., & Gidley, M. J. (2015). Rheology and microstructure characterisation of small intestinal digesta from pigs fed a red meat-containing Western-style diet. *Food Hydrocolloids*, 44, 300–308.
- Simulia, A. V. (2013). 6.13 Documentation. (Dassault systems).
- Singh, H., Ye, A., & Ferrua, M. J. (2015). Aspects of food structures in the digestive tract. *Current Opinion in Food Science*, 3, 85–93.
- Skamniotis C. Characterising and modelling fracture in functional pet foods (Doctoral dissertation, Imperial College London).
- Skamniotis, C. G., & Charalambides, M. N. (2020 Sep 11). Development of computational design tools for characterising and modelling cutting in ultra soft solids. *Extreme Mechanics Letters* 100964.
- Skamniotis, C. G., Patel, Y., Charalambides, M. N., & Elliott, M. (2016). Fracture investigation in starch-based foods. *Interface Focus*, 6(3), 20160005.
- Skamniotis, C. G., Elliott, M., & Charalambides, M. N. (2017). On modeling the large strain fracture behaviour of soft viscous foods. *Physics of Fluids*, 29(12), 121610.
- Skamniotis, C. G., Kamaludin, M. A., Elliott, M., & Charalambides, M. N. (2017 May 19). A novel essential work of fracture experimental methodology for highly dissipative materials. *Polymer*, 117, 167–182.
- Skamniotis, C. G., Patel, Y., Elliott, M., & Charalambides, M. N. (2018). Toughening and stiffening of starch food extrudates through the addition of cellulose fibres and minerals. *Food Hydrocolloids*, 84, 515–528.
- Skamniotis, C., Elliott, M., & Charalambides, M. (2019). On modelling the constitutive and damage behaviour of highly non-linear bio-composites–mesh sensitivity of the viscoplastic-damage law computations. *International Journal of Plasticity*, 114, 40–62.
- Skamniotis, C. G., Elliott, M., & Charalambides, M. N. (2019). Computer simulations of food oral processing to engineer teeth cleaning. *Nature Communications*, 10(1), 3571.
- Sozer, N., Cicerelli, L., Heinö, R.-L., & Poutanen, K. (2014). Effect of wheat bran addition on *in vitro* starch digestibility, physico-mechanical and sensory properties of biscuits. *Journal of Cereal Science*, 60(1), 105–113.
- Stokes, J. R., Boehm, M. W., & Baier, S. K. (2013 Aug 1). Oral processing, texture and mouthfeel: From rheology to tribology and beyond. *Current Opinion in Colloid & Interface Science*, 18(4), 349–359.
- Takahashi, T., & Sakata, T. (2002). Large particles increase viscosity and yield stress of pig cecal contents without changing basic viscoelastic properties. *The Journal of Nutrition*, 132(5), 1026–1030.
- Tanner, R. I., Qi, F., & Dai, S.-C. (2008). Bread dough rheology and recoil: I. rheology. *Journal of Non-Newtonian Fluid Mechanics*, 148(1–3), 33–40.
- Walter-Sack, I., De Vries, J., Nickel, B., Stenzhorn, G., & Weber, E. (1989). The influence of different formula diets and different pharmaceutical formulations on the systemic availability of paracetamol, gallbladder size, and plasma glucose. *International Journal of Clinical Pharmacology, Therapy, and Toxicology*, 27(11), 544–550.
- Wu, P., Dhital, S., Williams, B. A., Chen, X. D., & Gidley, M. J. (2016). Rheological and microstructural properties of porcine gastric digesta and diets containing pectin or mango powder. *Carbohydrate Polymers*, 148, 216–226.
- Xue, Z., Pontin, M., Zok, F., & Hutchinson, J. W. (2010). Calibration procedures for a computational model of ductile fracture. *Engineering Fracture Mechanics*, 77(3), 492–509.
- Yoo, J. Y., & Chen, X. D. (2006). GIT physicochemical modeling—a critical review. *International Journal of Food Engineering*, 2(4), 1–10.